

**1 Deoxygenation and its drivers analyzed in steady state
2 for perpetually slower and warmer oceans**

3 Benoît Pasquier¹, Mark Holzer¹,

4 Matthew A. Chamberlain², Richard J. Matear²,

5 and Nathaniel L. Bindoff³

6 ¹School of Mathematics and Statistics, University of New South Wales, Sydney, NSW, Australia

7 ²Commonwealth Scientific and Industrial Research Organisation, Hobart, TAS, Australia

8 ³Australian Antarctic Program Partnership, Institute for Marine and Antarctic Studies, University of

9 Tasmania, Hobart, TAS, Australia

10 Key Points:

- 11** • Key drivers of deoxygenation are quantified for oxygen cycles idealized by being
in equilibrium with perpetually slower oceans
- 12** • Widespread intense abyssal ocean deoxygenation is driven predominantly by slower
circulations allowing respiration to act over longer times
- 13** • Most of the reduction in preformed oxygen is driven by changes in ventilation pat-
terns and not by warming-driven reduced solubility

Corresponding author: Benoît Pasquier, b.pasquier@unsw.edu.au

Corresponding author: Mark Holzer, mholzer@unsw.edu.au

17 **Abstract**

18 The deoxygenation of the ocean is an important consequence of climate change that poses
19 an imminent threat to marine life and global food security. However, our understand-
20 ing of the complex interactions between changes in circulation, solubility, and respiration
21 that drive global-scale deoxygenation is incomplete. Here, we consider idealized bio-
22 geochemical steady states in equilibrium with perpetually slower and warmer oceans con-
23 structed from climate-model simulations of the 2090s that we hold constant in time. In
24 contrast to simulations of the end-of-century transient state, our idealized states are in-
25 tensely deoxygenated in the abyss, consistent with perpetually reduced ventilation and
26 Antarctic Bottom Water formation. We disentangle the effects of the deoxygenation drivers
27 on preformed oxygen and true oxygen utilization (TOU) using the novel concept of up-
28 stream exposure time, which precisely connects TOU to oxygen utilization rates and pre-
29 formed oxygen to ventilation. For our idealized steady states, deoxygenation below 2000 m
30 depth is due to increased TOU, driven dominantly by the slower circulations that allow
31 respiration to act roughly 2–3 times longer thereby overwhelming the effects of reduced
32 respiration rates. Above 500 m depth, decreased respiration and slower circulation closely
33 compensate, resulting in little expansion of upper-ocean hypoxia. The bulk of preformed
34 oxygen loss is driven by ventilation shifting equatorward to where warmer surface wa-
35 ters hold less oxygen. Warming-driven declines in solubility account for less than 10 %
36 of the total oxygen loss. Although idealized, our analysis suggests that long-term changes
37 in the marine oxygen cycle could be driven dominantly by changes in circulation rather
38 than by thermodynamics or biology.

39 **Plain Language Summary**

40 Climate change is driving oxygen out of the ocean, threatening marine life and global
41 food security. However, the precise contributions of the chemical, physical, and biolog-
42 ical processes that control oxygen levels are not well known because of their complex in-
43 teractions. To get a sense of these interactions, we consider idealized simulations of a global
44 oxygen cycle that is fully equilibrated with a perpetually warmer and slower ocean con-
45 structed from climate-model simulations of the 2090s but held constant in time for our
46 analyses. Compared to typical predictions, these idealized states exhibit intense deep ocean
47 deoxygenation, for which we precisely quantify the contributions from changes in solu-
48 bility, respiration, and ocean circulation. We find that deep-ocean deoxygenation is driven

49 by a slower circulation that allows respiration to act for more than twice as long over-
 50 coming lower respiration rates. The surface origin of oxygen shifts away from cold high-
 51 latitude waters toward warmer waters, in which atmospheric oxygen is less soluble, fur-
 52 ther reducing oxygen levels. Warming-driven decreases in solubility alone only account
 53 for a mere 10 % of the total oxygen loss. The upper ocean remains well oxygenated be-
 54 cause changes in respiration and circulation compensate almost perfectly. Our results
 55 highlight the central importance of circulation in controlling oxygen in the ocean.

56 1 Introduction

57 The ocean has lost an estimated ~1–3 % of its oxygen content over the last 50 years
 58 (e.g., Keeling & Garcia, 2002; Whitney et al., 2007; Helm et al., 2011; Schmidtko et al.,
 59 2017; Breitburg et al., 2018; Bindoff et al., 2022; Roach & Bindoff, 2023; Ito et al., 2017;
 60 Ito, 2022; Ito et al., 2024). Open-ocean deoxygenation is expected to continue in the fu-
 61 ture because of global warming, which reduces oxygen solubility and deep-ocean venti-
 62 lation (e.g., Matear et al., 2000; Keeling et al., 2010; Matear & Hirst, 2003; Bopp et al.,
 63 2013; Long et al., 2019; Oschlies, 2021). There is broad consensus among models of the
 64 sixth Coupled Model Intercomparison Project (CMIP6) that hypoxic zones will expand
 65 over the next century (e.g., in the Pacific; Busecke et al., 2022) to varying degrees de-
 66 pending on the future emissions' scenario (e.g., Kwiatkowski et al., 2020).

67 Ocean deoxygenation is increasingly recognized as posing an imminent threat to
 68 global marine ecosystems and food security (e.g., Earle et al., 2018; Laffoley & Baxter,
 69 2019). Oxygen is essential for life (e.g., Falkowski & Godfrey, 2008). Long-term expo-
 70 sure to sufficiently low oxygen (severe hypoxia) can be lethal to marine organisms (e.g.,
 71 Vaquer-Sunyer & Duarte, 2008; Diaz & Rosenberg, 2008). Mild to intermediate hypoxia
 72 has important physiological, behavioral, and ecological effects on marine ecosystems (e.g.,
 73 Ekau et al., 2010; Beman & Carolan, 2013; McCormick & Levin, 2017; Pascal et al., 2023;
 74 Morée et al., 2023). Hence, the distribution of oxygen in the ocean is a key control on
 75 shaping marine habitats (e.g., Rogers, 2000; Seibel, 2011; Stramma et al., 2012; Deutsch
 76 et al., 2015; Sato et al., 2017; Franco et al., 2022; Mongwe et al., under review; Deutsch
 77 et al., 2024). Even small O₂ declines and limited expansion of oxygen minimum zones
 78 (OMZs) are a major concern for global-ocean health (e.g., Gallo & Levin, 2016; Wish-
 79 ner et al., 2018; Deutsch et al., 2024).

80 Deoxygenation is driven by complex interactions among physical and biogeochemical
81 processes that interact non-linearly on global scales. Oxygen in the ocean is controlled
82 by air-sea exchange through surface winds and O₂ solubility, by photosynthetic produc-
83 tion in the surface ocean, by bacterial respiration, and by the circulation which venti-
84 lates the ocean and connects these processes through the transport of dissolved oxygen
85 to the deep ocean (e.g., Oschlies et al., 2018; Levin, 2018). To attribute O₂ changes quan-
86 titatively to specific driving mechanisms, a typical approach is to partition dissolved O₂
87 concentrations into a saturation concentration and apparent oxygen utilization (AOU;
88 e.g., Bopp et al., 2002; Schmidtko et al., 2017; Couespel et al., 2019; Long et al., 2019;
89 Busecke et al., 2022; Takano et al., 2023). To correct for AOU biases propagated by in-
90 complete surface O₂ saturation (Ito et al., 2004), another common approach (using mod-
91 els) is to compute preformed oxygen and “true” oxygen utilization (TOU; e.g., Oschlies
92 et al., 2019; Palter & Trossman, 2018; Buchanan & Tagliabue, 2021; Cliff et al., 2021;
93 Ito et al., 2022). Studies based on these approaches agree qualitatively that increased
94 oxygen utilization drives most of the deoxygenation, with reduced solubility accounting
95 for less than 50 % of upper-ocean deoxygenation, and less than ~25 % of the deoxygenation
96 of the entire water column. However, how much of the AOU (or TOU) increase can
97 be attributed to changes in ventilation (i.e., circulation) versus respiration remains un-
98 clear (e.g., Breitburg et al., 2018; Oschlies et al., 2018).

99 While the importance of circulation for open-ocean hypoxia was recognized long
100 ago (e.g., Wyrtki, 1962; Sarmiento et al., 1988), its precise contribution to changes in pre-
101 formed O₂ and oxygen utilization has yet to be quantified (Oschlies et al., 2018). This
102 is a challenging task because disentangling the effects of circulation changes from the ef-
103 fects of changes in solubility and upstream respiration requires a careful accounting of
104 all possible oxygen pathways and losses. To avoid these difficulties, some studies resort
105 to perturbation experiments, under the tacit assumption that the system is sufficiently
106 linear to infer the thermal and physical contributions to deoxygenation from the differ-
107 ence between perturbed and unperturbed simulations. These perturbed simulations may
108 consist, for example, in keeping surface solubility fixed in time (e.g., Matear et al., 2000;
109 Matear & Hirst, 2003; Couespel et al., 2019), in keeping oxygen utilization rates (OUR)
110 fixed in time (e.g., Deutsch et al., 2006), in removing biogeochemical processes (e.g., Cliff
111 et al., 2021), or in a combination of the above (e.g., Plattner et al., 2001; Bopp et al.,
112 2002). To assess circulation control on oxygen loss, other perturbations consist in keep-

113 ing the circulation fixed in its preindustrial state (e.g., Palter & Trossman, 2018). Such
 114 residual-based perturbation approaches can be strongly biased by spatial correlations be-
 115 tween changes in solubility and changes in circulation that are typically ignored. How-
 116 ever, as we show here, such correlations can be of first order for large perturbations or
 117 over long timescales. Also commonly used for assessing the effects of circulation changes
 118 on deoxygenation is the ideal mean age, often invoked as an empirical timescale linking
 119 TOU and OUR (e.g., Bopp et al., 2017; Palter & Trossman, 2018; Busecke et al., 2022).
 120 However, all the studies mentioned here ultimately fall short of accurately attributing
 121 deoxygenation to its drivers because they lack a quantitative framework, based on the
 122 underlying fundamental equations, that connects TOU to OUR with the correct circu-
 123 lation timescale.

124 Here, we focus on idealized steady-state biogeochemistry that is in equilibrium with
 125 frozen-in-time ocean circulations. We can thus probe the oxygen cycle on all the funda-
 126 mental timescales of the associated ocean transport (e.g., fast thermocline versus slow
 127 abyssal ventilation). In particular, our approach captures the very longest timescales that
 128 cannot be probed with typical centennial-scale transient simulations. In addition, steady
 129 states afford many computational advantages that we exploit extensively. However, be-
 130 cause of the frozen-in-time nature of our ocean states, natural variability on any timescale
 131 is not captured (e.g., seasonal, interannual). For the reference steady state, we use prein-
 132 dustrial conditions. For the idealized states embedded in warmer and slower oceans, we
 133 use decadal-mean circulations of the 2090s, all as simulated by the Australian Commu-
 134 nity Climate and Earth System Simulator (ACCESS1.3; Bi et al., 2013). We hold these
 135 circulations fixed in time for perpetuity, embed the intermediate-complexity PCO₂ bio-
 136 geochemistry model (Pasquier, Holzer, Chamberlain, Matear, et al., 2023), and solve for
 137 the biogeochemical steady state using a quasi Newton's method. Our idealized biogeo-
 138 chemical steady states exhibit intense abyssal deoxygenation because of the perpetually
 139 reduced ventilation and Antarctic Bottom Water (AABW) formation (Holzer et al., 2020),
 140 which stands in stark contrast to typical transient simulations of the late 21st century.
 141 While our idealized states cannot capture realistic transient evolution, they neverthe-
 142 less inform us on the long-timescale mechanisms that drive deoxygenation.

143 We rigorously partition O₂ changes into contributions from circulation changes, sol-
 144 ubility changes, and their spatial correlations by employing the exact timescale that con-
 145 nects TOU to upstream OUR. Specifically, in steady state, the local OUR contribution

146 at location \mathbf{r} to the TOU content of an interior volume Ω has recently been shown to
 147 be $\text{OUR}(\mathbf{r}) \times \Gamma_{\Omega}^{\uparrow}(\mathbf{r})$, where $\Gamma_{\Omega}^{\uparrow}(\mathbf{r})$ is the “upstream exposure time”, i.e., the time that
 148 the water in Ω spent sweeping past upstream location \mathbf{r} , and hence the time over which
 149 $\text{OUR}(\mathbf{r})$ acts (Holzer, 2022). Importantly, $\Gamma_{\Omega}^{\uparrow}$ is a fundamental timescale of the circu-
 150 lation only. Furthermore, we show here that $\Gamma_{\Omega}^{\uparrow}$ also connects the preformed O_2 content
 151 of Ω to its surface origin.

152 We find that the intense abyssal deoxygenation in our idealized steady states is char-
 153 acterized by widespread expansion of mild to severe hypoxia. Above 500 m depth, hy-
 154 poxic regions do not expand appreciably because decreases in preformed oxygen are com-
 155 pensated by colocated TOU reductions, driven primarily by reduced respiration rates.
 156 Below 2000 m depth, by contrast, strong increases in TOU are predominantly driven by
 157 the slower perpetual 2090s circulation allowing respiration to act over 2 to 3 times longer.
 158 Preformed oxygen declines almost everywhere, driven primarily by equatorward shifts
 159 in ventilation caused by reduced AABW and North Atlantic Deep Water (NADW) for-
 160 mation, with reduced solubility only playing a secondary role (order 10 % of the total
 161 oxygen loss). Our analyses highlight the overarching importance of the circulation in de-
 162 termining the ocean’s oxygen content through its control on ventilation patterns and the
 163 path-integrated oxygen utilization.

164 2 Methods

165 2.1 Frozen-in-time preindustrial and 2090s ocean circulations

166 We consider a preindustrial and two idealized ocean states that are frozen in time.
 167 Specifically, we use simulations from the Australian Community Climate and Earth Sys-
 168 tem Simulator (ACCESS1.3; Marsland et al., 2013; Bi et al., 2013) and average their ocean
 169 circulation and thermodynamic state variables (including temperature and salinity), which
 170 we hold constant for perpetuity. The 1990s decadal average is used as an approximately
 171 preindustrial state, and the 2090s decadal average is used to represent warmer and slower
 172 ocean states, corresponding to an intermediate and a worst-case climate-change scenario
 173 (Representative Concentration Pathways RCP4.5 and RCP8.5; Meinshausen et al., 2011,
 174 2020). For further details, see the work of Pasquier, Holzer, and Chamberlain (2023),
 175 who used the same framework of steady-state biogeochemistry embedded in frozen-in-
 176 time circulations to quantify carbon-pump changes.

177 We emphasize that we do not assume that our perpetual-2090s circulations cor-
178 responds to a steady state of the ocean dynamics. Instead, we simply freeze the mean
179 2090s ocean state in time and analyze the resulting idealized steady-state oxygen cycle
180 that would be in equilibrium with this perpetually slower and warmer ocean. Our re-
181 sults thus cannot be interpreted as predictions of the future. However, despite the caveats
182 of our idealized framework (Section 4.1), our results inform us on the key mechanisms
183 that drive deoxygenation in the real ocean. Our steady states capture the biogeochemical
184 response on the longest timescales, avoid the complications of transience, which sim-
185 plifies our analysis and facilitates decomposing and separating the drivers of deoxygenation,
186 and remove the need for time stepping, which is computationally advantageous.

187 The advective–diffusive flux-divergence operator of each state is organized into a
188 sparse transport matrix following Chamberlain et al. (2019). The horizontal advective
189 fluxes were directly averaged from the ACCESS1.3 output while the vertical advective
190 fluxes were inferred from mass conservation by integrating the horizontal divergence up-
191 ward from the seafloor. Horizontal and vertical diffusion is included in the transport ma-
192 trix with background diffusivities of $500 \text{ m}^2 \text{ s}^{-1}$ and $10^{-5} \text{ m}^2 \text{ s}^{-1}$, and in the mixed layer
193 there is strong vertical diffusion at $0.1 \text{ m}^2 \text{ s}^{-1}$. For this purpose we used the decadal mean
194 of the yearly maximum mixed-layer depth as simulated by ACCESS1.3. The model grid
195 employed (coarse-grained from the original ACCESS1.3 grid) has a nominal horizontal
196 resolution of $2^\circ \times 2^\circ$ (finer in the tropics) and 50 vertical levels with thicknesses increas-
197 ing from 10 m at the surface to 335 m at depth. We used the same horizontal and ver-
198 tical diffusivities for the preindustrial and 2090s states, and all the quantities calculated
199 herein include both advection and diffusion.

200 When interpreting our results below it is important to note that like most state-
201 of-the-art climate models, the ACCESS1.3 circulation features an unrealistically deep
202 mixed layer in the Southern Ocean compared to observations (de Boyer Montégut et al.,
203 2004; Bi et al., 2013; de Lavergne et al., 2014). For the ACCESS1.3 simulations we used,
204 the mixed layers reach below 5000 m near the Weddell and Ross Seas in the 1990s and
205 strongly shoal in the 2090s, which imprints on our results (as in Pasquier, Holzer, & Cham-
206 berlain, 2023). Although abyssal ventilation and bottom-water formation through con-
207 vection are unrealistic (e.g., Heuzé et al., 2013), the key realistic model behavior for our
208 purposes here is a decline in Southern Ocean deep ventilation driven by climate change:
209 Antarctic Bottom Water formation has been observed to decline in recent decades and

210 is predicted to decline strongly over the next few decades (e.g., de Lavergne et al., 2014;
 211 Chen et al., 2023; Gunn et al., 2023; Li et al., 2023). (Detailed caveats of the circula-
 212 tion model are discussed in Section 4.1.)

213 **2.2 Oxygen model**

214 For the oxygen cycle, we use the PCO2 biogeochemistry model of Pasquier, Holzer,
 215 Chamberlain, Matear, et al. (2023). PCO2 is embedded in the frozen-in-time ocean cir-
 216 culations using our transport matrices, and we solve directly for the biogeochemical steady
 217 state using a quasi Newton’s Method. Our steady-state oxygen cycles thus correspond
 218 to the equilibrium that would ultimately be reached if the thermodynamic and physi-
 219 cal state of the ocean were held at its 2090s level in perpetuity.

220 A key feature of PCO2 for capturing the response of dissolved oxygen to climate
 221 change is that PCO2 explicitly models the nonlinear interactions and feedbacks between
 222 oxygen, carbon, and nutrients. This includes the effects of oxygen and particulate or-
 223 ganic matter on respiration, and the effects of temperature on biological production and
 224 respiration. The biogeochemical parameters of PCO2 were objectively optimized for prein-
 225 dustrial conditions against observations of phosphate, dissolved inorganic carbon, total
 226 alkalinity, and oxygen. (The same parameter values were then used for all our states.)
 227 Oxygen in the optimized state has a global volume-weighted root-mean-square model–
 228 observations mismatch of $\sim 30 \mu\text{M}$ (Pasquier, Holzer, Chamberlain, Matear, et al., 2023).
 229 Systematic biases, in part inherited from the parent ACCESS-model circulation, remain
 230 despite parameter optimization, with underestimated O_2 in the upper tropical Pacific
 231 and Atlantic above $\sim 1000 \text{ m}$ and overestimated O_2 in the Southern Ocean and the trop-
 232 ical Indian Ocean (see Appendix Fig. A1 for a comparison between modelled and observed
 233 zonal mean $p\text{O}_2$). However, we deem these biases acceptable as they are smaller than
 234 for most CMIP5 models (Bao & Li, 2016) and because they are generally dwarfed by the
 235 much larger changes analyzed here.

236 In the PCO2 model, oxygen enters and exits the ocean through air-sea gas exchange,
 237 is photosynthetically produced in the euphotic layer, and is utilized through aerobic bac-
 238 terial respiration. In steady state, the three-dimensional O_2 concentrations obeys

239
$$\mathcal{T} \text{O}_2 = P - \text{OUR} + J_{\text{atm}}, \quad (1)$$

where the frozen-in-time transport operator \mathcal{T} acts on O_2 concentrations such that $\mathcal{T}O_2 = \nabla \cdot (\mathbf{u}O_2) - \nabla \cdot \mathbf{K} \nabla O_2$ is the flux divergence of O_2 due to advection (with velocity \mathbf{u}) and eddy diffusion (diffusivity tensor \mathbf{K}). $P = r_{O_2:C} U_C$ is the photosynthetic production of oxygen keyed to biological carbon uptake U_C through the optimized $r_{O_2:C} = 1.31 \text{ molO}_2 \text{ molC}^{-1}$, and $\text{OUR} = r_{O_2:C} (R_{\text{DOC}} + R_{\text{POC}}) \Theta(O_2 - O_2^{\text{lim}})$ is the oxygen utilization rate keyed to respiration of dissolved and particulate organic carbon (R_{DOC} and R_{POC}). (The Θ term switches off aerobic respiration when O_2 drops below $O_2^{\text{lim}} = 5 \mu\text{M}$, implicitly representing the effect of anaerobic denitrification.) Air-sea gas exchange is modelled using the parameterization $J_{\text{atm}} = k (K_0 pO_2^{\text{atm}} - O_2) / h$ at the surface (Wanninkhof, 2014), where k is the wind- and temperature-dependent gas-transfer velocity, K_0 is the temperature- and salinity-dependent oxygen solubility, pO_2^{atm} is the oxygen atmospheric partial pressure (based on an atmospheric oxygen mixing ratio of 0.210 for both preindustrial and perpetual-2090s states), and $h = 10 \text{ m}$ is the thickness of the top model layer. (See Section 4.1 for discussion on the caveats of the biogeochemistry model.)

We organize the grid values of concentrations into column vectors and discretized linear operators into corresponding sparse matrices. The nonlinear system of biogeochemical tracer equations is solved for steady state using a quasi Newton's method. In matrix form, the vector of oxygen, \mathbf{O}_2 , is the solution to $\mathbf{T} \mathbf{O}_2 = \mathbf{P} - \mathbf{OUR} + \mathbf{J}_{\text{atm}}$, where \mathbf{T} is the discretized advective-diffusive flux-divergence operator ("transport matrix" for short) such that $\mathbf{T} \mathbf{O}_2$ is the vector of the oxygen flux-divergence, and \mathbf{P} , \mathbf{OUR} , and \mathbf{J}_{atm} are the vectors of photosynthetic oxygen production, oxygen utilization, and air-sea oxygen exchange, respectively.

2.3 Preformed oxygen, O_2^{pre}

Preformed oxygen is defined here as the oxygen that would be propagated by the ocean circulation out of the euphotic-layer and into the ocean's interior in the absence of any aphotic sources and sinks. We use the base of the euphotic zone rather than the base of the mixed layer to define preformed oxygen for convenience and consistency with the definitions of preformed and regenerated phosphate and carbon in the related work of Pasquier, Holzer, Chamberlain, Matear, et al. (2023) and Pasquier, Holzer, and Chamberlain (2023). Hence, O_2^{pre} depends only on euphotic O_2 concentrations and on ventilation patterns.

271 In matrix form, the vector of preformed oxygen, $\mathbf{O}_2^{\text{pre}}$, is conveniently computed
 272 by solving $(\mathbf{T}+\mathbf{L}) \mathbf{O}_2^{\text{pre}} = \mathbf{L} \mathbf{O}_2$, where \mathbf{L} is a diagonal matrix with diagonal values of
 273 1 s^{-1} in the euphotic zone and 0 otherwise, enforcing $\mathbf{O}_2^{\text{pre}} = \mathbf{O}_2$ in the euphotic zone (only
 274 the euphotic-zone values of \mathbf{O}_2 are used in $\mathbf{L} \mathbf{O}_2$). (For such short (1 s) relaxation times
 275 there is no sensitivity to the precise value of that relaxation time; for example, using 10 s
 276 would give indistinguishable results.)

277 To separate the effects of solubility from the effects of circulation on \mathbf{O}_2 within the
 278 euphotic zone, we further decompose $\mathbf{O}_2^{\text{pre}}$ into a saturated component $\mathbf{O}_2^{\text{sat}}$ and a dis-
 279 equilibrium component $\mathbf{O}_2^{\text{dis}} = \mathbf{O}_2^{\text{pre}} - \mathbf{O}_2^{\text{sat}}$. This decomposition is useful because the
 280 air-sea \mathbf{O}_2 disequilibrium varies with location and can be important in deep-water for-
 281 mation regions (see, e.g., Russell & Dickson, 2003; Ito et al., 2004; Duteil et al., 2013;
 282 Eggleston & Galbraith, 2018).

283 2.4 True oxygen utilization, TOU

284 To quantify the oxygen deficit caused by loss to respiration, we use “true oxygen
 285 utilization” $\text{TOU} = \mathbf{O}_2^{\text{pre}} - \mathbf{O}_2$ (e.g., Broecker & Peng, 1982; Ito et al., 2004; Koeve & Käh-
 286 ler, 2016; Holzer, 2022). TOU is thus the cumulated amount of oxygen that has been
 287 removed by respiration along its interior transit since leaving the euphotic zone. The vec-
 288 tor of TOU grid values is computed similarly to preformed \mathbf{O}_2 by solving $(\mathbf{T}+\mathbf{L}) \mathbf{TOU} =$
 289 \mathbf{OUR} (Holzer, 2022). Note that $-\text{TOU}$ may also be thought of as regenerated oxygen,
 290 $\mathbf{O}_2 - \mathbf{O}_2^{\text{pre}}$ (e.g., DeVries & Deutsch, 2014).

291 2.5 Deoxygenation drivers

292 To summarize the contributions from changes in circulation, solubility, or respi-
 293 ration, it is useful to integrate the oxygen change over a specific subvolume Ω of interest.
 294 We will first consider TOU and then $\mathbf{O}_2^{\text{pre}}$.

295 2.5.1 Change in TOU

296 The Ω inventory of TOU is controlled at every location \mathbf{r} upstream of Ω by $\text{OUR}(\mathbf{r})$
 297 and by the time that the water currently in Ω spent flowing past \mathbf{r} , which is the time
 298 for which $\text{OUR}(\mathbf{r})$ acts on the oxygen heading toward Ω . This timescale, which we call
 299 “upstream exposure time” here, was only recently computed by Holzer (2022), who showed

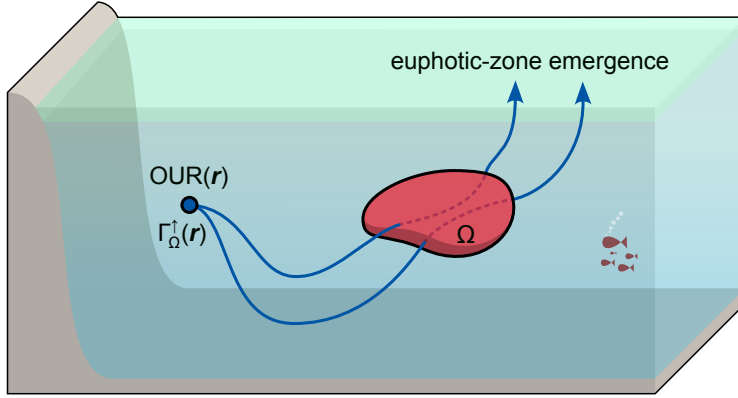


Figure 1. The upstream exposure time at any interior location \mathbf{r} (blue dot) is the time that water currently in interior volume Ω (red region) spent at \mathbf{r} in the past (integrated over all pathways and past times; blue lines). It is thus the total time for which the water in Ω was exposed to oxygen utilization at upstream location \mathbf{r} in the past. This allows us to connect the oxygen “missing” in Ω (the Ω -integrated TOU) to the oxygen utilization rate (OUR) at \mathbf{r} . In steady state, this upstream exposure time equals $\Gamma_\Omega^\uparrow(\mathbf{r})$, the mean time that water currently at location \mathbf{r} will spend in Ω on its way to the euphotic zone (see also Eq. (2) and Holzer, 2022).

300 that for steady flow it is equal to $\Gamma_\Omega^\uparrow(\mathbf{r})$, the mean time that water currently at \mathbf{r} will
 301 spend in Ω on its way to the surface (see Fig. 1). In steady state, $\Gamma_\Omega^\uparrow(\mathbf{r})$ equals the time
 302 that oxygen at \mathbf{r} was exposed to respiration upstream of Ω and connects the TOU in-
 303 ventory to OUR(\mathbf{r}) through the relationship (Holzer, 2022):

304

$$\int_{\Omega} \text{TOU}(\mathbf{r}) d^3\mathbf{r} = \int \text{OUR}(\mathbf{r}) \Gamma_\Omega^\uparrow(\mathbf{r}) d^3\mathbf{r}. \quad (2)$$

305 We emphasize that the upstream exposure time (Γ_Ω^\uparrow in steady state) is fundamentally
 306 different from the ideal mean age (e.g., Primeau, 2005), which is commonly used to ap-
 307 proximate relate TOU or AOU to OUR (e.g., Doney & Bullister, 1992; Warner et al.,
 308 1996; Zheng et al., 1997; Feely et al., 2004; Bopp et al., 2017; Palter & Trossman, 2018,
 309 to cite a few), despite known systematic biases (e.g., Duteil et al., 2013; Sonnerup et al.,
 310 2013; Brandt et al., 2015; Sonnerup et al., 2015; Koeve & Kähler, 2016; Thomas et al.,
 311 2020).

312 The integrals in Eq. (2) are easily computed in matrix form. That is, Eq. (2) can
 313 be written as $\boldsymbol{\Omega}^\top \mathbf{V} \text{TOU} = \text{OUR}^\top \mathbf{V} \boldsymbol{\Gamma}_\Omega^\uparrow$, where \mathbf{V} is a diagonal matrix with the grid-
 314 box volumes along the diagonal, $\boldsymbol{\Omega}$ is a mask vector with entries of 1 for grid cells in Ω
 315 and entries of 0 otherwise, and the $^\top$ superscript denotes the matrix transpose. The up-

316 stream exposure time obeys $(\tilde{\mathbf{T}} + \mathbf{L}) \boldsymbol{\Gamma}_\Omega^\uparrow = \boldsymbol{\Omega}$ (Holzer, 2022), where $\tilde{\mathbf{T}} = \mathbf{V}^{-1} \mathbf{T}^\top \mathbf{V}$ is
 317 the volume-weighted adjoint of the transport matrix that governs the time-reversed ad-
 318 joint flow.

319 The quantitative connection of TOU with OUR through $\boldsymbol{\Gamma}_\Omega^\uparrow$ in Eq. (2) allows us to
 320 partition TOU changes into contributions from changes in respiration, circulation, and
 321 their interaction. Specifically, we algebraically decompose, at every point \mathbf{r} of the ocean,
 322 the change in the integrand ($\text{OUR} \times \boldsymbol{\Gamma}_\Omega^\uparrow$) on the right-hand-side of Eq. (2) as

$$323 \quad \Delta(\text{OUR} \times \boldsymbol{\Gamma}_\Omega^\uparrow) = \underbrace{\boldsymbol{\Gamma}_\Omega^\uparrow \Delta\text{OUR}}_{\text{respiration}} + \underbrace{\text{OUR} \Delta\boldsymbol{\Gamma}_\Omega^\uparrow}_{\text{circulation}} + \underbrace{\Delta\text{OUR} \Delta\boldsymbol{\Gamma}_\Omega^\uparrow}_{\text{cross term}}, \quad (3)$$

324 where a quantity X not preceded by Δ denotes its preindustrial value and ΔX denotes
 325 the change in X for the state embedded in the perpetual-2090s circulations. The driv-
 326 ing process represented by each term is indicated beneath the braces of Eq. (3), and these
 327 terms are globally integrated to give the corresponding contributions to the changes in
 328 the Ω inventory of TOU in accord with Eq. (2). The $\boldsymbol{\Gamma}_\Omega^\uparrow \Delta\text{OUR}$ term corresponds to the
 329 contribution from respiration-only changes, with the circulation fixed at its preindustrial
 330 state, while $\text{OUR} \Delta\boldsymbol{\Gamma}_\Omega^\uparrow$ corresponds to the contribution from circulation-only changes,
 331 with OUR fixed at its preindustrial value, and the “cross term” $\Delta\text{OUR} \Delta\boldsymbol{\Gamma}_\Omega^\uparrow$ corresponds
 332 to the simultaneous colocated changes in OUR and upstream exposure time. To the best
 333 of our knowledge, this is the first decomposition to cleanly separate respiration-only and
 334 circulation-only effects, and to explicitly account for the effect of simultaneous changes
 335 in both respiration and circulation.

336 2.5.2 Change in O_2^{pre}

337 In steady state, the Ω inventory of preformed oxygen is determined by euphotic oxy-
 338 gen concentrations modulated by the amount of Ω -volume ventilated per unit area at
 339 the base of the euphotic zone, $\mathcal{V}_\Omega^\downarrow$. Mathematically,

$$340 \quad \int_\Omega \text{O}_2^{\text{pre}}(\mathbf{r}) d^3\mathbf{r} = \int \text{O}_2(\mathbf{r}_s) \mathcal{V}_\Omega^\downarrow(\mathbf{r}_s) d^2\mathbf{r}_s, \quad (4)$$

341 where location \mathbf{r}_s ranges over the base of the euphotic layer. The matrix form of Eq. (4)
 342 is $\boldsymbol{\Omega}^\top \mathbf{V} \boldsymbol{O}_2^{\text{pre}} = \boldsymbol{O}_2^\top \mathbf{A} \mathcal{V}_\Omega^\downarrow$ where \mathbf{A} is a diagonal matrix with the horizontal area of each
 343 grid cell along the diagonal and where $\mathcal{V}_\Omega^\downarrow = \mathbf{A}^{-1} \mathbf{L} \mathbf{V} \boldsymbol{\Gamma}_\Omega^\uparrow$. One can derive these re-
 344 lationships by noting that just like OUR is the source term for TOU , the equation for
 345 preformed oxygen shows that $\mathbf{L} \boldsymbol{O}_2$ is the effective source term for $\boldsymbol{O}_2^{\text{pre}}$. By replacing

346 **OUR** with $\mathbf{L} \mathbf{O}_2$ and **TOU** with $\mathbf{O}_2^{\text{pre}}$ in the matrix form of Eq. (2), we obtain $\boldsymbol{\Omega}^T \mathbf{V} \mathbf{O}_2^{\text{pre}} =$
347 $\mathbf{O}_2^T \mathbf{L} \mathbf{V} \boldsymbol{\Gamma}_{\Omega}^{\uparrow}$. This relationship provides a direct connection between the $\mathbf{O}_2^{\text{pre}}$ inventory
348 of Ω and the flux of $\boldsymbol{\Gamma}_{\Omega}^{\uparrow}$ into the euphotic zone, because $\boldsymbol{\Gamma}_{\Omega}^{\uparrow}$ traces the $\mathbf{O}_2^{\text{pre}}$ currently in
349 Ω back to its euphotic origin. (We note in passing that this link stems from the equiv-
350 alence between mixing ratio propagated forward in time from a boundary condition and
351 the flux into that boundary from a unit-injected mass propagated in the time-reversed
352 adjoint flow (e.g., Holzer & Hall, 2000).)

353 The Ω volume ventilated per unit area $\mathcal{V}_{\Omega}^{\downarrow}$ is a generalization of the ocean volume
354 ventilated per unit area (e.g., Primeau, 2005; Holzer et al., 2020). We note that $\mathcal{V}_{\Omega}^{\downarrow}$ is
355 also proportional to the volume fractions f_{ij} derived by Fu et al. (2018) for quantifying
356 the ventilation of OMZs, through $f_{ij} = A_{ij} \mathcal{V}_{\Omega}^{\downarrow} / v_{\Omega}$, where A_{ij} is the surface grid cell
357 area and v_{Ω} is the Ω volume. This can be seen by rewriting the matrix version of Eq. (4)
358 as $\boldsymbol{\Omega}^T \mathbf{V} \mathbf{O}_2^{\text{pre}} = \mathbf{O}_2^T \mathbf{V} \mathbf{f}_{\Omega}^{\downarrow}$ where $\mathbf{f}_{\Omega}^{\downarrow}$ is the vector of the fractional Ω volume ventilated
359 by each euphotic-zone grid cell used in the work of Fu et al. (2018). What is new and
360 important here is the quantitative connection between the Ω inventory of $\mathbf{O}_2^{\text{pre}}$ and eu-
361 photic \mathbf{O}_2 concentrations provided by $\mathcal{V}_{\Omega}^{\downarrow}$.

362 Similar to our analysis of TOU changes, we partition changes in the Ω inventory
363 of $\mathbf{O}_2^{\text{pre}}$ into contributions from changes in solubility and circulation. To this end, we al-
364gebraically decompose, at every point \mathbf{r}_s at the base of the euphotic layer, the change
365 in the integrand $\mathbf{O}_2 \mathcal{V}_{\Omega}^{\downarrow}$ on the right-hand-side of Eq. (4) as

$$\Delta(\mathbf{O}_2 \mathcal{V}_{\Omega}^{\downarrow}) = \underbrace{\mathcal{V}_{\Omega}^{\downarrow} \Delta \mathbf{O}_2^{\text{sat}}}_{\text{solubility}} + \underbrace{\mathbf{O}_2^{\text{sat}} \Delta \mathcal{V}_{\Omega}^{\downarrow}}_{\text{circulation}} + \underbrace{\Delta(\mathbf{O}_2^{\text{dis}} \mathcal{V}_{\Omega}^{\downarrow})}_{\text{cross term}}, \quad (5)$$

366 where we have further separated euphotic \mathbf{O}_2 into its saturated and disequilibrium com-
367 ponents and the driving process represented by each term is indicated beneath the braces.
368 The term $\mathcal{V}_{\Omega}^{\downarrow} \Delta \mathbf{O}_2^{\text{sat}}$ accounts for the contribution to $\Delta \mathbf{O}_2^{\text{pre}}$ in Ω from solubility-only changes
369 by keeping the circulation (and thus ventilation volumes $\mathcal{V}_{\Omega}^{\downarrow}$) fixed in its preindustrial
370 state. The contribution from circulation-only changes includes $\mathbf{O}_2^{\text{sat}} \Delta \mathcal{V}_{\Omega}^{\downarrow}$, where solubil-
371 ity in the euphotic zone is fixed at its preindustrial values, and $\Delta(\mathbf{O}_2^{\text{dis}} \mathcal{V}_{\Omega}^{\downarrow})$, which we con-
372sider to be a circulation-only effect by assuming that $\mathbf{O}_2^{\text{dis}}$ is entirely driven by circula-
373tion changes. The decomposition of Eq. (5) is, to the best of our knowledge, also new.

375 **2.6 Hypoxia severity categories**

376 To quantify the extent of low-oxygen conditions, we follow Hofmann et al. (2011)
 377 and define hypoxia categories A, B, and C, ranging from mild to severe in terms of the
 378 in situ effective partial pressure of oxygen, pO_2 . Specifically for our model, category-A
 379 mild hypoxia is deemed to occur where $pO_2 \leq 100$ matm, category-B intermediate hy-
 380 poxia where $pO_2 \leq 50$ matm, and category-C severe hypoxia where $pO_2 \leq 15$ matm.
 381 Note that we have adjusted the $pO_2 = 106, 60$, and 22 matm thresholds of Hofmann
 382 et al. (2011) such that the modelled global hypoxia volume for each category matches
 383 the values based on GLODAPv2 observations (Lauvset et al., 2016). Despite matching
 384 the global hypoxic volumes, the horizontal extent of hypoxic regions remain overestimated
 385 in the Pacific and Atlantic and underestimated in the Indian Ocean (see Appendix Figs. A2
 386 and A3 for more details).

387 **3 Results**388 **3.1 Global deoxygenation and expansion of hypoxic regions**

389 We find intense deoxygenation for our steady-state oxygen cycles embedded in the
 390 perpetual-2090s ocean states, with the global oxygen inventory decreasing by 30 % and
 391 60 % for the RCP4.5- and RCP8.5-based states, respectively. Figure 2 shows the basin
 392 zonal-mean pO_2 for each scenario and the corresponding change from preindustrial to
 393 perpetual-2090s states. (We show the effective partial pressure, pO_2 , because it is the
 394 most relevant thermodynamic oxygen quantity for critical physiological processes in liv-
 395 ing organisms (Hofmann et al., 2011).) The oxygen loss is largest in the Pacific because
 396 of the dramatically reduced ventilation from AABW. Oxygen loss is also intense in the
 397 Atlantic sector of the Southern Ocean, but deoxygenation in the Atlantic is overall less
 398 pronounced as the mid-depth North Atlantic remains ventilated by North Atlantic Deep
 399 Water (NADW) in the perpetual-2090s circulations. Deoxygenation does not occur ev-
 400 erywhere however, with slight increases in the zonal mean pO_2 occurring close to the sur-
 401 face in each basin, particularly at northern mid-latitudes in the Atlantic and Indian Ocean
 402 (Fig. 2j–o), likely due to reduced local respiration and shoaling NADW.

403 The expansion of hypoxic zones depends strongly on the severity (i.e., pO_2 thresh-
 404 old) of hypoxia considered, on the local ventilation, and on the climate-change scenario.
 405 Figure 3 shows the profiles of the spatial extent of each hypoxia category (Methods, Sec-

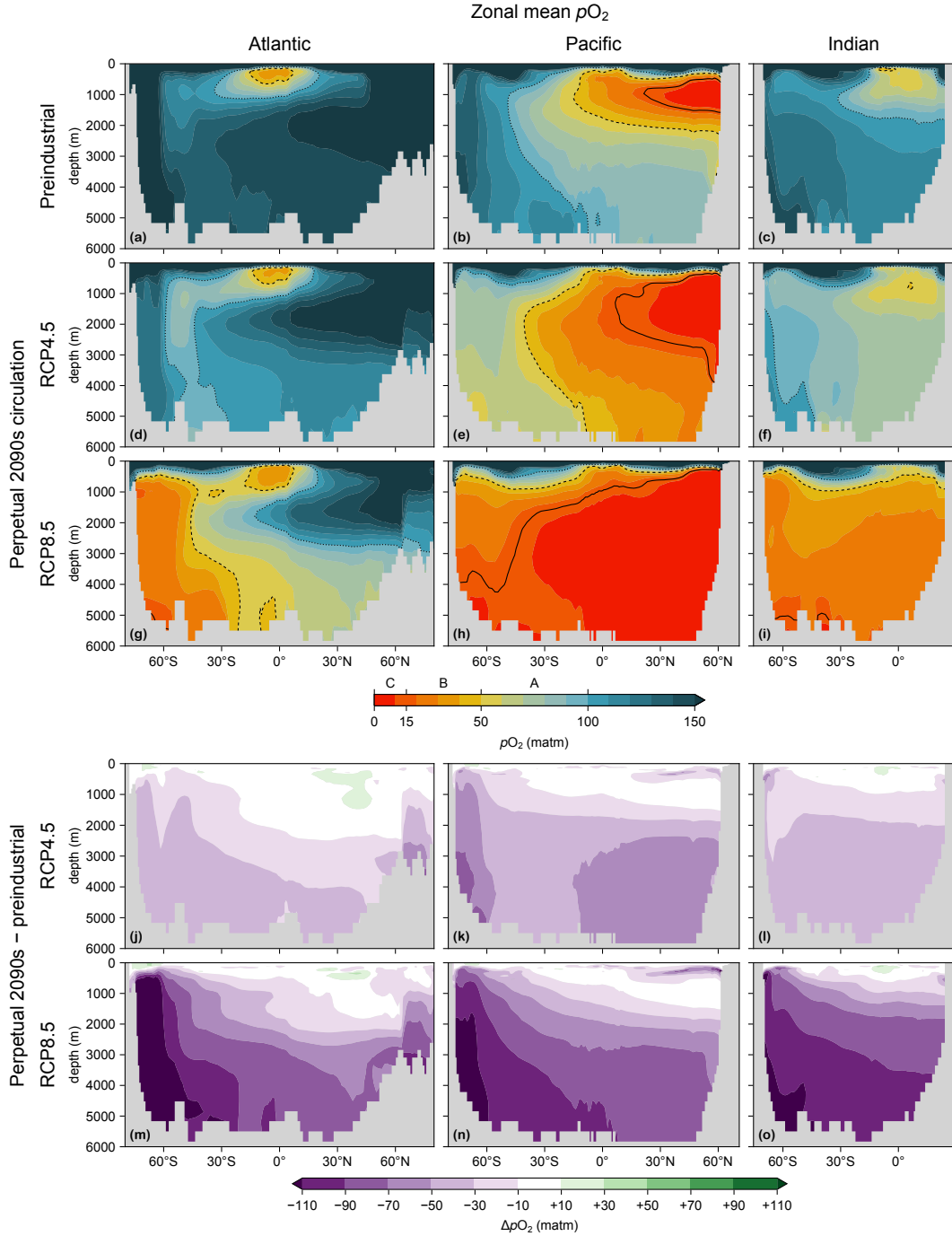


Figure 2. (a) Atlantic, (b) Pacific, and (c) Indian Ocean zonal-mean $p\text{O}_2$ for the preindustrial state. The dotted, dashed, and solid contour lines indicate the $p\text{O}_2 = 100, 50$, and 15 matm thresholds of hypoxia categories A, B, and C, respectively. (d–f) As (a–c) for the state with perpetual-2090s circulation of the RCP4.5 scenario. (g–i) As (d–f) for RCP8.5. (j–o) As (d–i) for the change from the preindustrial state to the perpetual-2090s states. The Atlantic basin excludes the Gulf of Mexico and the Caribbean, and the Pacific basin excludes the Sea of Japan so that the zonal means are more cleanly interpretable.

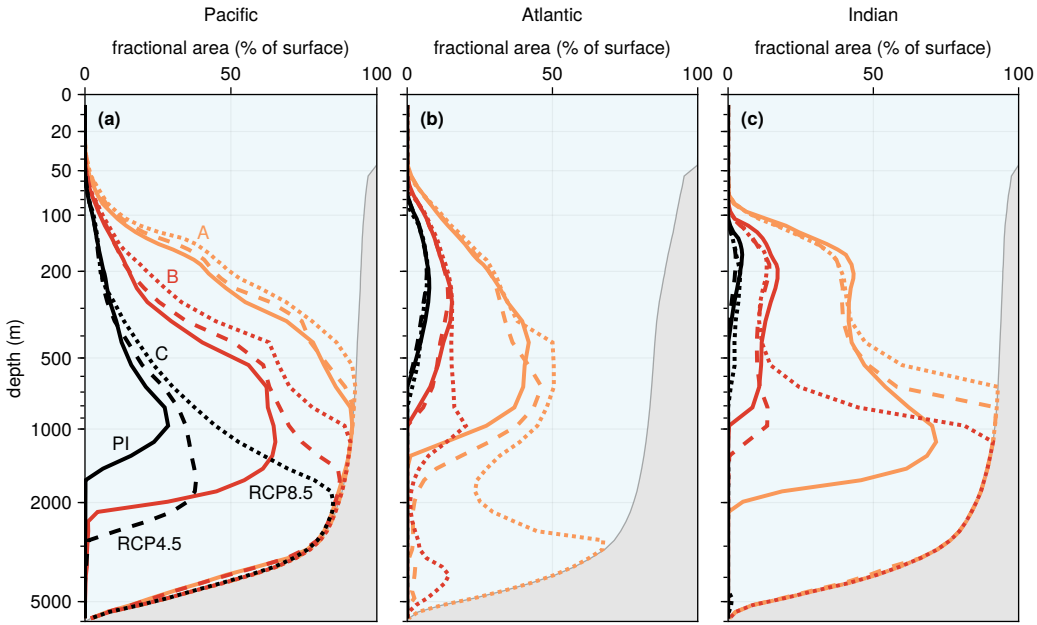


Figure 3. (a) Pacific depth profiles of the spatial extent of mild (A, orange; $pO_2 \leq 100$ matm), intermediate (B, red; $pO_2 \leq 50$ matm), and severe hypoxia (C, black; $pO_2 \leq 15$ matm) for the preindustrial state (PI; solid lines), the perpetual RCP4.5 2090s state (dashed lines), and the perpetual RCP8.5 2090s state (dotted lines). The spatial extent for a given hypoxia category and depth is quantified by the ratio of the horizontal hypoxic area to the surface area of the corresponding ocean basin. (The gray area represents the seafloor.) (b) As (a) for the Atlantic. (c) As (a) for the Indian Ocean. Note the nonlinear depth scale.

406 tion 2.6), over each basin, and for each scenario. The expansion of hypoxic regions is larger
 407 for RCP8.5 than for the less extreme RCP4.5 scenario. We find that low-oxygen condi-
 408 tions generally expand toward the seafloor in the deep ocean rather than toward the sur-
 409 face. In the Pacific, expansion is maximal with all abyssal waters becoming moderately
 410 hypoxic (cat. B; $pO_2 \leq 50$ matm) for RCP4.5 and severely hypoxic (cat. C; $pO_2 \leq 15$ matm)
 411 for RCP8.5. Similarly, all Indian Ocean waters below roughly 800 m become mildly hy-
 412 poxic for RCP4.5 and moderately hypoxic for RCP8.5. In the Atlantic, the volume of
 413 severe hypoxia changes little, while mild and intermediate hypoxia only strongly expand
 414 for RCP8.5 at intermediate and abyssal depths. In the Atlantic and Indian Ocean above
 415 500 m, the areal extent of hypoxia actually contracts slightly as pO_2 has slight increases
 416 there (cf., Fig. 2j-o discussed above).

To visualize the horizontal distribution of expanding hypoxic conditions, we consider the vertical water-column minimum pO_2 shown in Fig. 4. In the preindustrial state, oxygen minimum zones are located in the eastern tropical sectors of the major basins and in the North Pacific. In the perpetual-2090s states, global-scale expansion of low-oxygen conditions is visible for RCP4.5, except in the North Atlantic and in the Atlantic sector of the Southern Ocean, which remain ventilated ($pO_2 \geq 100$ matm) by NADW and AABW. Intermediate hypoxia expands southward beyond southern mid-latitudes, while severe hypoxia expands into the tropics. For the RCP8.5-based state, mild hypoxia occurs across the entire global ocean (although predominantly at depth as shown in Fig. 3), while intermediate hypoxia occurs across the entire Pacific, South Atlantic, and Indian Ocean, and severe hypoxia extends across the entire Pacific only, reaching as far as the Southern Ocean.

3.2 Drivers of deoxygenation

3.2.1 Changes in TOU and preformed oxygen

Deoxygenation occurs through declines in preformed oxygen and through increases in true oxygen utilization (TOU; see Methods, Section 2), which may also be thought of as negative regenerated oxygen (i.e., $O_2^{\text{reg}} = -\text{TOU}$; see, e.g., DeVries & Deutsch, 2014). Qualitatively, reduced respiration drives TOU decreases while a slower circulation drives TOU increases by allowing more time for respiration to act. Thus, TOU can either increase or decrease (Appendix Fig. B1) depending on which effect dominates. We find that in the upper ocean TOU decreases because of reduced OUR and in the deep ocean TOU increases because of longer circulation timescales (upstream exposure times; Appendix Fig. B2). Preformed oxygen, by contrast, declines over most of the ocean (Appendix Fig. B1), in part because of warming-driven solubility decreases and importantly, as we will show below, because of an equatorward shift in ventilation. With warmer future sea surface temperature (SST), surface O_2 concentrations decrease almost everywhere, except in the North Atlantic “cold blob” (e.g., Cheng et al., 2022) where temperatures decrease, and near the Weddell and Ross Seas where the mixed layer shoals (Appendix Fig. B3). Shoaling of the ACCESS model’s preindustrially deep mixed layer in these regions (see Fig. C2 in Pasquier, Holzer, Chamberlain, Matear, et al., 2023) considerably increases surface residence times, allowing preindustrially undersaturated O_2

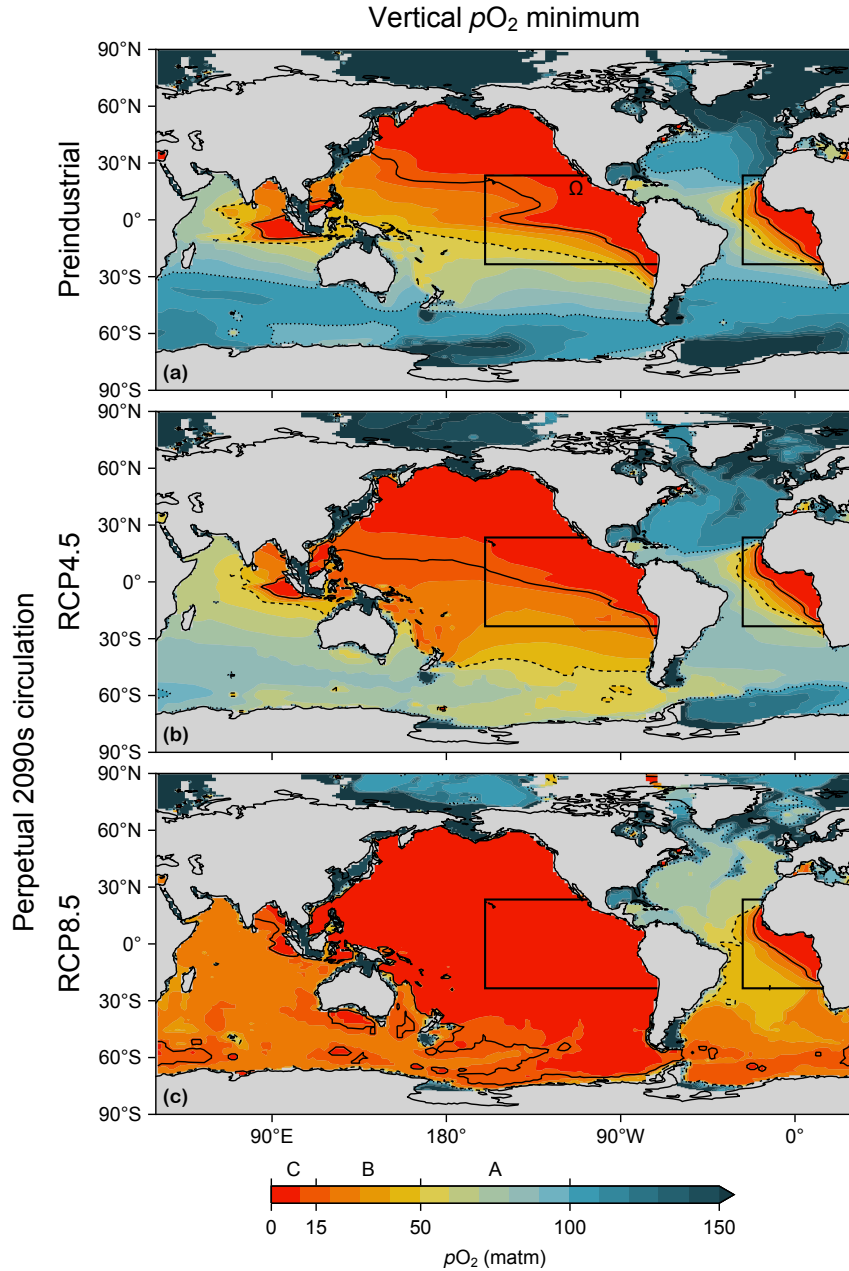


Figure 4. (a–c) Maps of the water-column minimum $p\text{O}_2$ for (a) the preindustrial state, (b) the perpetual-2090s RCP4.5 state, and (c) the perpetual-2090s RCP8.5 state. The dotted, dashed, and solid contour lines indicate the $p\text{O}_2 = 100$, 50, and 15 matm thresholds of hypoxia categories A, B, and C, respectively. Also indicated are the eastern tropical Pacific and Atlantic Ω regions over which our diagnostics are applied.

448 to become more saturated despite the decreased solubility. (See Section 4.1 for caveats
 449 on the circulation model.)

450 To analyze the drivers of deoxygenation in detail, we focus for definiteness on the
 451 eastern tropical Pacific (ETP, 23°S–23°N, east of 160°W) and eastern tropical Atlantic
 452 (ETA, 23°S–23°N, east of 27°W), as indicated in Fig. 4. Figure 5 shows the average O_2
 453 depth profiles in these regions and their decomposition into O_2^{pre} and TOU. In the prein-
 454 dustrial state, both the ETP and ETA are severely hypoxic in the depth range of 150–800 m
 455 and 150–400 m, respectively. In the perpetual-2090s steady states, we find small upper-
 456 ocean O_2 decreases of about 10 μM above 70 m, caused by a decrease in O_2^{pre} . Decreases
 457 in O_2^{pre} are approximately constant with depth below \sim 100 m, while ΔTOU changes sign
 458 at \sim 1500 m in the ETP and at \sim 800 m in the ETA. Above \sim 500 m, the TOU decreases
 459 compensate almost perfectly for the O_2^{pre} decreases. Conversely, below \sim 2000 m, TOU
 460 increases and O_2^{pre} decreases compound, resulting in strong deoxygenation, with deep
 461 ETP O_2 reduced to \sim 25 % of its preindustrial levels for RCP4.5 and to a mere \sim 5 % for
 462 RCP8.5. Deep ETA O_2 decreases are of similar magnitude, but O_2 levels are roughly 100 μM
 463 higher in all states owing to North Atlantic ventilation.

464 We now partition the changes ΔTOU and ΔO_2^{pre} into contributions from the key
 465 drivers, that is, into contributions from changes in circulation, respiration, and solubil-
 466 ity (Methods, Section 2.5). For this purpose, we narrow our focus to the ETP only —
 467 similar mechanisms are at play in the ETA, but will not be discussed here for brevity.
 468 Guided by the shape of their profiles in Fig. 5, we furthermore integrate over the upper
 469 ETP (above 500 m) and separately over the deep ETP (below 2000 m) to summarize how
 470 different drivers dominate at different depths. (For simplicity, we use the surface rather
 471 than the mixed- or euphotic-layer base as the top boundary of the upper ETP so that
 472 it occupies the same volume for all states.) The resulting attribution of ΔTOU and ΔO_2^{pre}
 473 to their drivers is shown in Fig. 6; we first discuss ΔTOU and then ΔO_2^{pre} .

474 3.2.2 Upper and deep ETP budgets of ΔTOU

475 The average TOU over a given region Ω is given by the global volume integral of
 476 the product of OUR with the upstream exposure time, Γ_Ω^\uparrow in steady state (see Methods,
 477 Section 2, Eq. (2), and Fig. 1). This allows us to decompose ΔTOU into contributions
 478 from changes in respiration, from changes in circulation, and from their spatial corre-

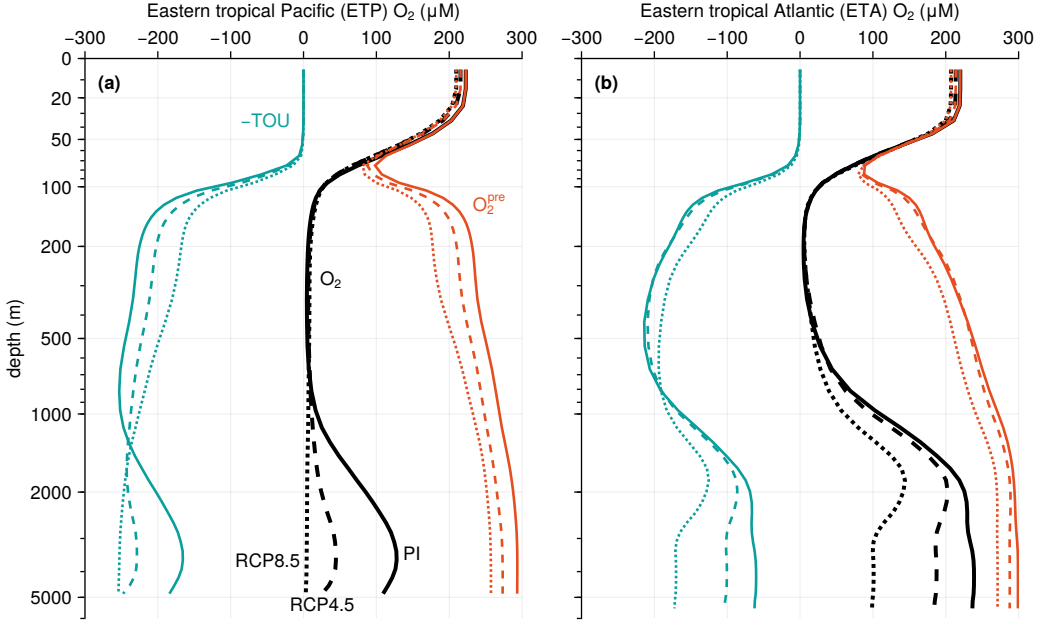


Figure 5. (a) Eastern tropical Pacific profiles of oxygen (O_2 , black), preformed oxygen (O_2^{pre} , orange), and true oxygen utilization (TOU, teal) for the preindustrial state (PI; solid line), the perpetual-2090s RCP4.5 state (dashed line), and the perpetual-2090s RCP8.5 state (dotted line). We show regenerated oxygen, $-TOU$, to show the effect of utilization on O_2 as additive. Note the nonlinear depth scale. (b) As (a) for the eastern tropical Atlantic. (The eastern tropical Pacific and Atlantic regions are defined in Fig. 4.)

lations, which we refer to as the “cross term” in Eq. (3). These contributions are shown as the first three colored bars in each panel of Fig. 6.

In general terms, Figure 6 shows that the global decline in respiration acts toward decreasing TOU (green bars; note that Fig. 6 shows $\Delta O_2^{reg} = -\Delta TOU$), and hence increasing O_2 everywhere, as expected. Conversely, the slower 2090s circulation increases TOU (blue bars) by increasing the upstream exposure time, allowing respiration, albeit at a reduced rate, to act over longer times. The magnitude of the cross-term contributions to ΔTOU (orange bars) are generally on the same order as the circulation-only and respiration-only contributions, partly because of the large changes considered here. Note that the ΔTOU cross term acts toward increasing O_2 because ΔOUR and $\Delta \Gamma_\Omega^\uparrow$ have opposite signs (negative contribution to ΔTOU). We now examine the drivers of TOU changes in detail for the upper and deep ETP.

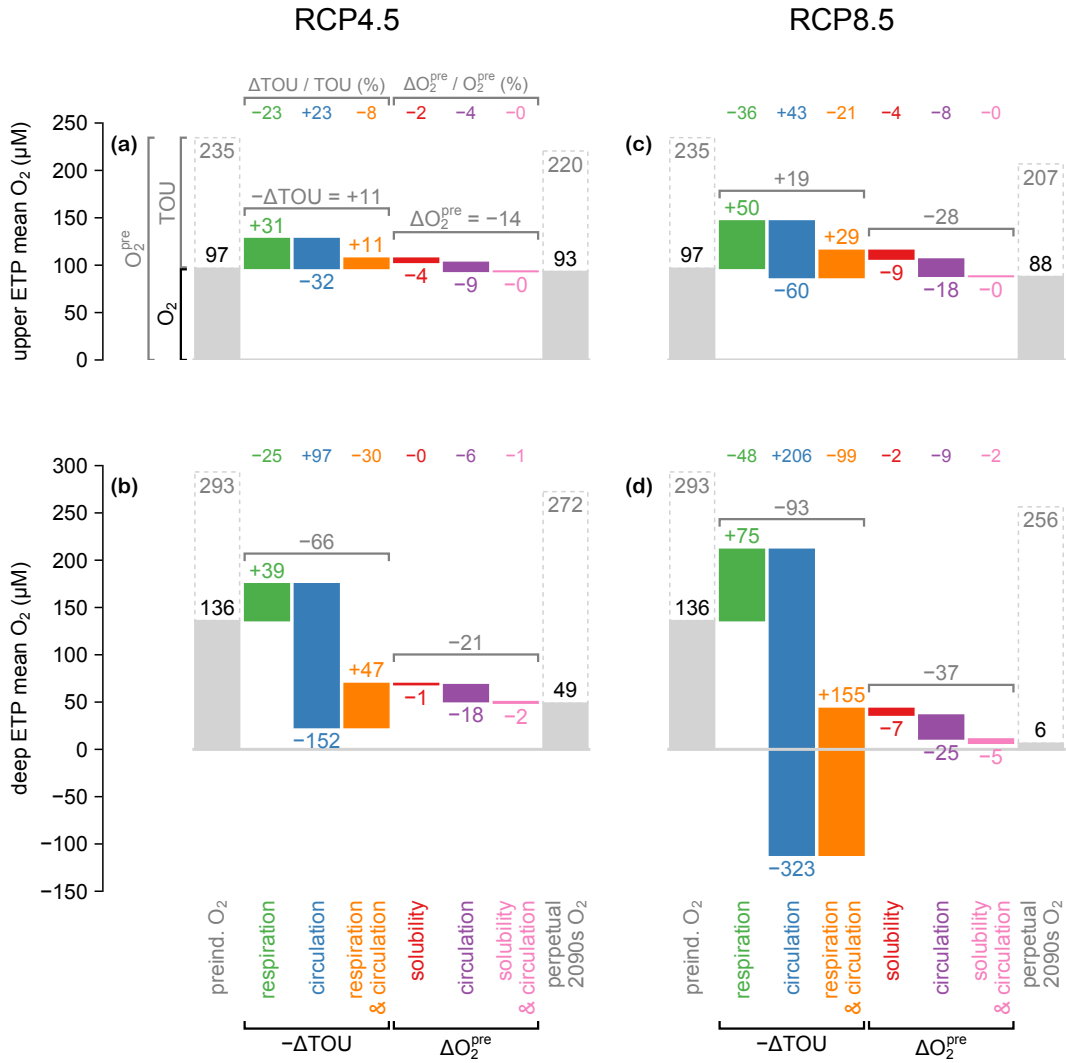


Figure 6. (a) ΔO_2 contributions for the upper ETP (0–500 m) for RCP4.5 plotted as a waterfall chart with the O_2 change from the preindustrial state (leftmost gray bar) to the perpetual-2090s state (rightmost gray bar) decomposed into contributions (colored bars) that start where the previous one ends. ΔTOU is decomposed according to Eq. (3) into contributions from changes in respiration (green), circulation (blue), and their spatial covariance (orange). ΔO_2^{pre} is decomposed into contributions from solubility (red), circulation (purple), and their spatial covariance (pink). Percentage contributions to changes in ΔTOU and ΔO_2^{pre} are indicated at the top. (b) As (a) for the deep ETP (below 2000 m). (c–d) As (a–b) for RCP8.5.

For the upper ETP (Fig. 6a,c), respiration-driven TOU reduction (green bar) is closely compensated by circulation-driven TOU increases (blue bar). This shows that in the upper ocean respiration is slower (driving TOU reductions of 23 % and 36 % for RCP4.5

and RCP8.5), but the slower circulation allows this respiration to act for longer (driving TOU increases of 23 % and 43 %). As the effects of respiration-only changes (green bars) and circulation-only changes (blue bars) nearly cancel, the overall TOU decrease is driven by the spatial correlation between respiration changes and circulation changes (orange bars). The concurrent increase of the circulation-only driven TOU and decrease of the respiration-only driven TOU must result in a negative cross term and hence in a TOU reduction, the precise magnitude of which depends on details of the underlying spatial patterns. The magnitude of the overall TOU decrease is about 8 % for RCP4.5 and 21 % for RCP8.5.

For the deep ETP, the circulation-only-driven ΔTOU (blue bars) dominates the other drivers with a magnitude that is roughly 5 times larger than for the upper ETP. In comparison, the magnitude of the respiration-only-driven ΔTOU (green bars) is only 30 % and 50 % larger for RCP4.5 and RCP8.5 than in the upper ETP. The respiration-driven decreases and circulation-driven increases in TOU again point to slower respiration acting for longer time. To quantify this, we calculated the upstream-exposure-time-weighted change in OUR and the OUR-weighted change in upstream exposure time to find that respiration slows by 25 % for RCP4.5 and 50 % for RCP8.5 but acts 2 times longer for RCP4.5 and 3 times longer for RCP8.5. For the deep ETP the cross terms (orange bars) are of the same order of magnitude as the respiration-only contribution (green bars), but the cross terms no longer dominate the overall TOU change as in the upper ETP. With all terms combined, the TOU of the deep ETP increases by 42 % for RCP4.5 and by 59 % for RCP8.5. A striking feature of these results is that, were respiration to be held constant at its preindustrial level, the ΔTOU contribution from the circulation slowdown alone (blue bars) is so strong that it would have the potential to remove the entire O_2 content of the deep ETP (filled gray bars) in the RCP4.5 scenario, and to do so more than two times over in the RCP8.5 scenario.

3.2.3 Upper and deep ETP budgets of $\Delta\text{O}_2^{\text{pre}}$

The preformed oxygen content of volume Ω is controlled by euphotic O_2 concentrations and by the amount of the Ω volume that is ventilated per unit area at the base of the euphotic layer, $\mathcal{V}_\Omega^\downarrow$ (see Methods, Section 2, Eq. (4)). While $\mathcal{V}_\Omega^\downarrow$ depends only on the circulation, euphotic O_2 concentration is determined by both solubility and circulation through the subtle balance between air-sea gas exchange and euphotic-zone res-

526 idence time. However, decomposing euphotic O_2 into saturation and disequilibrium com-
 527 ponents, O_2^{sat} and O_2^{dis} , allows us to separate solubility from circulation effects (includ-
 528 ing their spatial correlation “cross term” in Eq. (5)) because euphotic O_2^{sat} is determined
 529 by in situ solubility only, while euphotic O_2^{dis} is predominantly determined by circula-
 530 tion. These contributions, volume integrated over either the upper or deep ETP, are also
 531 plotted as colored bars in Fig. 6.

532 Reduced surface solubility reduces the preformed oxygen inventory of the ETP by
 533 just a few percent (red bars) even for the extreme RCP8.5 case, accounting for less than
 534 $\sim 30\%$ of the overall O_2^{pre} decrease in the upper and deep ETP. The bulk ($\sim 70\%$ or more)
 535 of the overall order-10% decline in preformed oxygen is instead driven by changes in cir-
 536 culation (purple bars). The cross terms (pink bars) between already relatively small solubility-
 537 only and circulation-only contributions are essentially negligible. The circulation-only
 538 driven reductions in O_2^{pre} due to $\Delta V_\Omega^\downarrow$ represent re-arrangements in euphotic origin be-
 539 cause the area integral of V_Ω^\downarrow , which equals the volume of Ω , is constant across all states.
 540 The decreases in the circulation-only contributions to ΔO_2^{pre} (computed with the prein-
 541 dustrial surface oxygen concentration) thus indicate a shift in ventilation pattern toward
 542 surface locations with lower oxygen concentration, i.e., toward warmer latitudes with lower
 543 solubility (see also Appendix Fig. B4). This equatorward shift in ventilation reduces the
 544 efficiency of the oxygen solubility pump and is the dominant driver of the decline in the
 545 preformed O_2 in both the upper and deep ETP.

546 It is interesting to note that regions with weaker ventilation have longer surface res-
 547 idence time and thus higher surface saturation, which can compensate for reduced sol-
 548 ubility. In our perpetual-2090s states this occurs near the Weddell and Ross seas where
 549 the deep preindustrial mixed layer shoals dramatically thereby increasing surface resi-
 550 dence and saturation, which overwhelm the effect of reduced solubility leading to increased
 551 surface oxygen concentrations.

552 ***3.2.4 TOU changes in the ETP: three-dimensional distribution of TOU 553 origin***

554 Having quantified the globally integrated drivers of ETP deoxygenation, we now
 555 investigate their spatial distribution, beginning with the local contributions to TOU. The
 556 local contribution at point r to the TOU inventory of region Ω is given by the product

557 $\Gamma_{\Omega}^{\uparrow}(\mathbf{r})$ OUR(\mathbf{r}), which quantifies the origin of the TOU inventory, i.e., the oxygen loss
 558 that occurred at \mathbf{r} upstream of Ω . Figures 7 and 8 show the TOU origin for the upper
 559 and deep ETP, respectively. The zonally integrated TOU origin is plotted for the prein-
 560 dustrial state together with the corresponding changes for the perpetual-2090s states.

561 For the upper ETP (Fig. 7), TOU originates almost exclusively in the Pacific, pre-
 562 dominantly in thermocline waters across all non-polar latitudes, with peak contributions
 563 at a depth of \sim 200 m. Thus, there is significant oxygen loss within the upper-ocean cir-
 564 culation as it transports oxygen to the upper ETP. TOU in the upper ETP also orig-
 565 inates at depths between 1000–2000 m at low and high latitudes, where upwelling old oxy-
 566 gen is intercepted by the bacterial respiration of abundant sinking organic matter be-
 567 neath high productivity. For both RCP4.5 and RCP8.5, the change in TOU origin re-
 568 veals a shoaling (upward shift) of the average location where oxygen bound for the up-
 569 per ETP is lost. This shift presumably occurs because the slower 2090s circulation al-
 570 lows respiration to act for longer so that oxygen bound for the upper ETP is stripped
 571 out higher in the water column. The TOU origin below the thermocline at low and high
 572 latitudes decreases, presumably because of reduced biological productivity and subja-
 573 cent respiration, as well as a lower O₂ content of the water that upwells there. The up-
 574 ward shift in TOU origin and reduced deep origin are thus both consequences of respi-
 575 ration removing oxygen sooner, i.e., further upstream, during its transit from the euphotic
 576 zone.

577 For the deep ETP (Fig. 8), TOU originates in every ocean basin. The Atlantic makes
 578 a 20 % contribution and the Indian Ocean a 15 % contribution, mostly at high latitudes
 579 known to ventilate the deep Pacific (e.g., Holzer et al., 2021). For all basins, the largest
 580 TOU origin lies in upper thermocline waters where most respiration occurs. Deeper TOU
 581 origin at high latitudes, and in the Pacific throughout the water column at low latitudes,
 582 occurs below regions of vigorous biological production where respiration is high. The fact
 583 that the low-latitude tongue of oxygen loss in the Pacific lies partly above, and hence
 584 *down-stream* of the deep ETP, implies that either some O₂ is utilized as it mixes diffu-
 585 sively downward, or, more likely, that water destined to be carried by meridional over-
 586 turning back to the deep ETP at depth has its oxygen stripped out in the upwelling branch
 587 of the overturning. Consistent with such an overturning pathway, local maxima of TOU
 588 origin occur in the mid-depth North Pacific and in the abyssal Pacific sector of the South-
 589 ern Ocean.

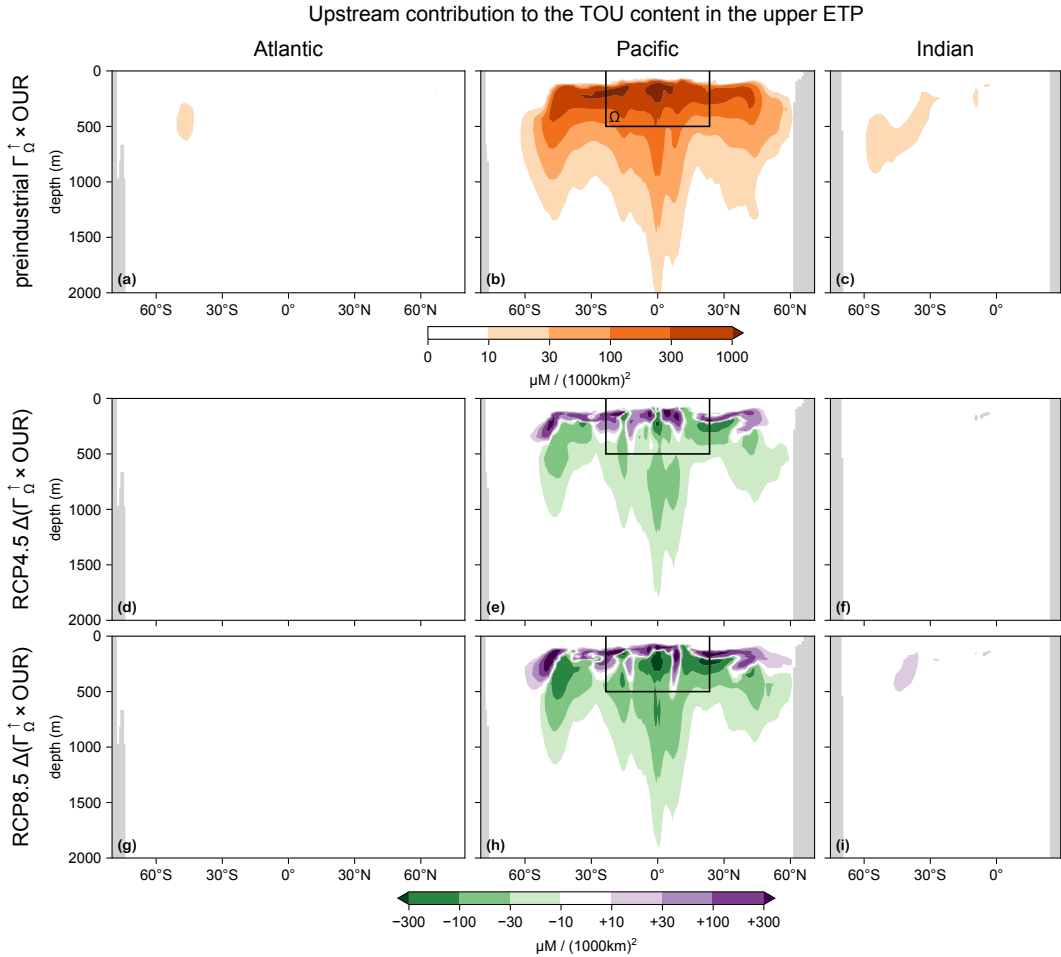


Figure 7. Preindustrial upstream contribution to the TOU in the upper ETP (0–500 m; indicated by the solid black line; subvolume Ω in our equations) as quantified by basin zonal integrals of $\Gamma_{\Omega}^{\uparrow} \times \text{OUR}$ normalized by the ETP volume for the Atlantic (a), Pacific (b), and Indian Ocean (c). (d–f) As (a–c) for the change from the preindustrial state to the perpetual-2090s state for the RCP4.5 scenario. (g–i) As (d–f) for RCP8.5. Note the nonlinear color scale and that the normalized zonal integrals plotted give the contribution per unit latitude–depth area.

The changes in the TOU origin of the deep ETP plotted in Fig. 8 show a global increase and upstream intensification of the removal of oxygen destined for the deep ETP. For the RCP4.5-based perpetual-2090s state, the TOU origin increases mostly near the surface of the Pacific, South Atlantic, and southern Indian Ocean where it was already large in the preindustrial state. For RCP8.5, the TOU contributions are generally stronger and, unlike for RCP4.5, they also increase near the North Atlantic surface. However, in the old waters of the mid-depth North Pacific the TOU origin of the deep ETP actually

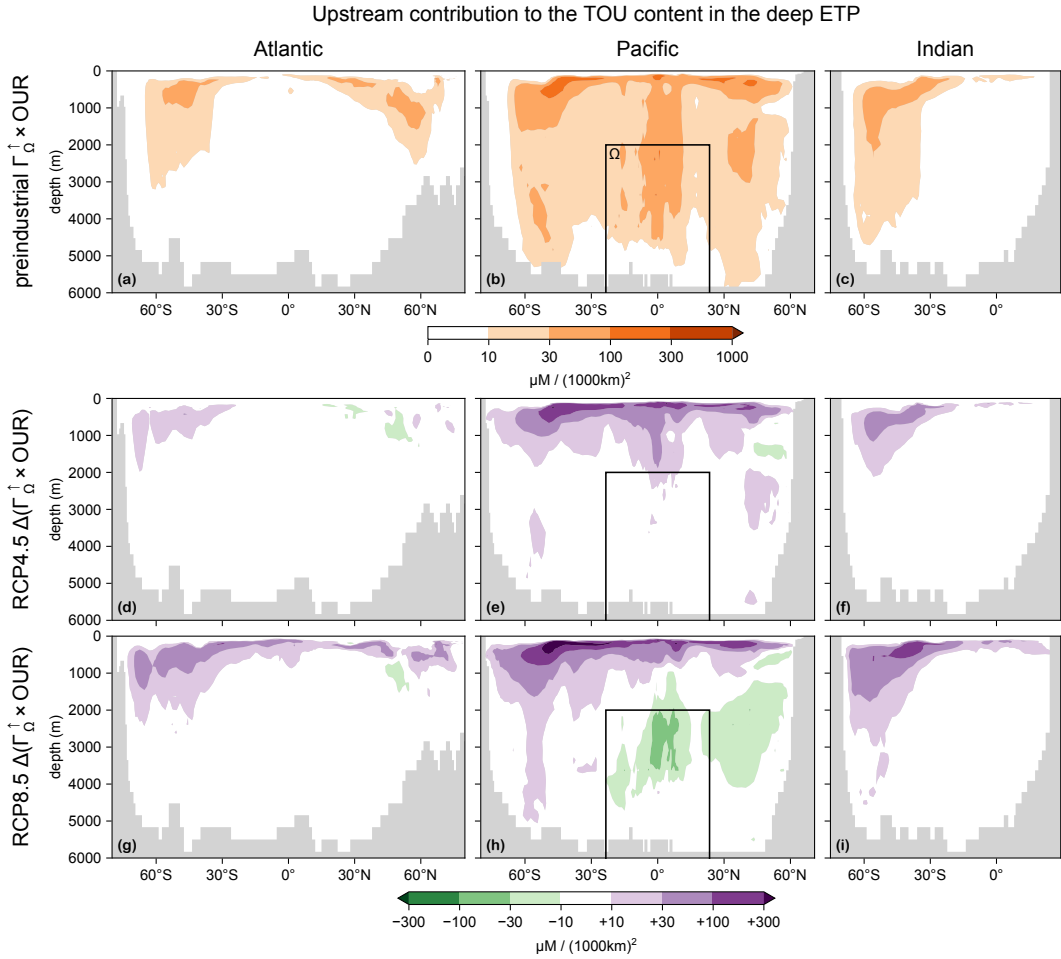


Figure 8. As Fig. 7 for the deep ETP (below 2000 m; indicated by the solid black line).

decreases for RCP8.5, likely because of shifts in production, and hence respiration, away from the surface origin of these old waters so that less oxygen is stripped out of them.

599 **3.2.5 Preformed oxygen changes in the ETP: shifting ventilation pat-**
 600 **terns**

601 Here we take a closer look at the geographic shifts in ventilation patterns that drive
 602 the decreased preformed oxygen content of the ETP. The amount of O_2^{pre} supplied to Ω
 603 from euphotic location r is quantified by the product $O_2(r) \mathcal{V}_\Omega^\downarrow(r)$, maps and zonal in-
 604 tegrals of which are plotted in Fig. 9 for the preindustrial state together with the changes
 605 for the perpetual-2090s states. (Corresponding plots of $\mathcal{V}_\Omega^\downarrow$ by itself, shown in Appendix
 606 Fig. B4, share strong similarities with Fig. 9, underscoring that changes in ventilation pat-
 607 terns are the dominant driver of ΔO_2^{pre} .)

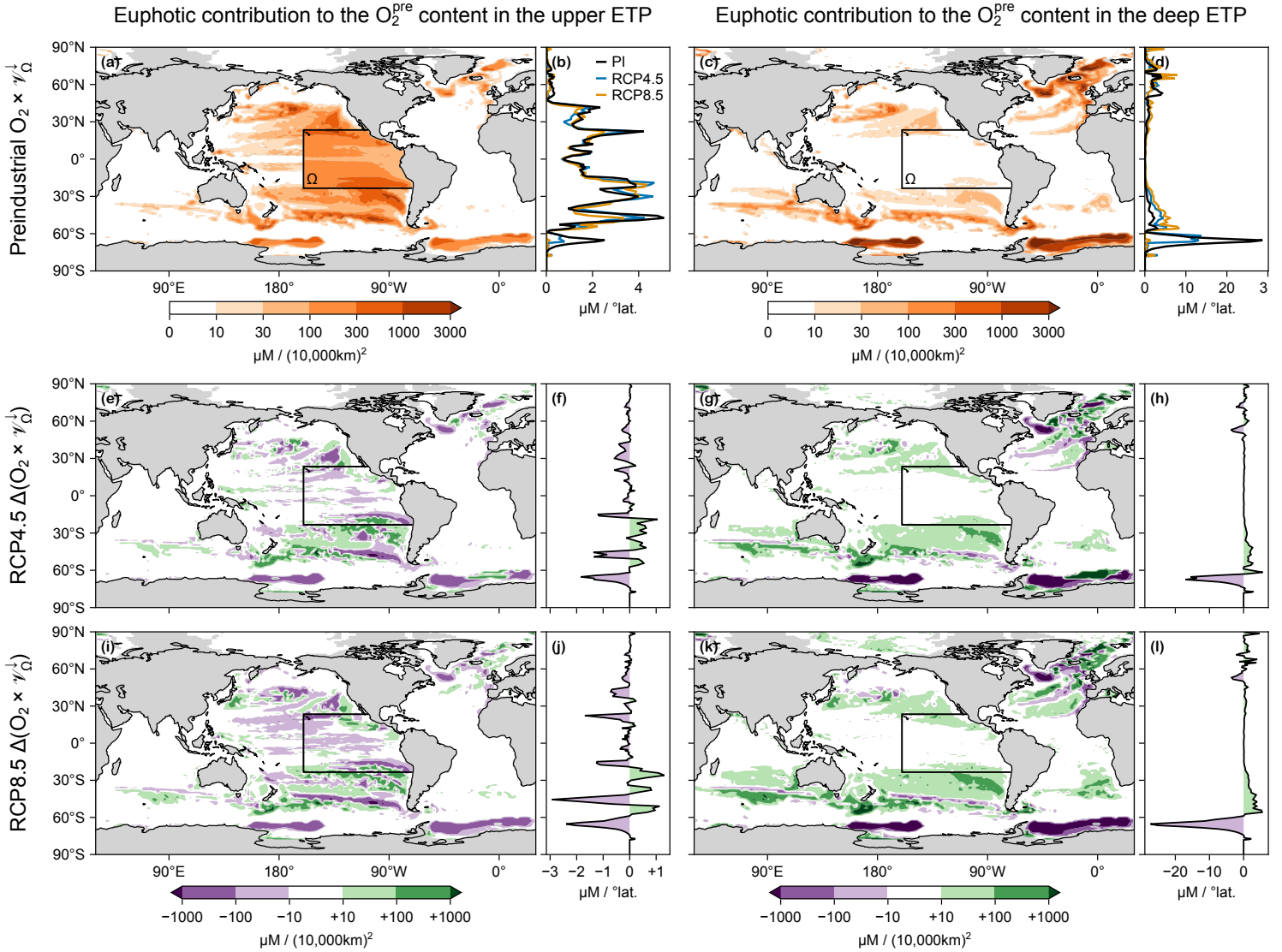


Figure 9. (a) Map and (b) zonal integral of the euphotic contribution to the mean O_2^{pre} in the upper ETP (subvolume Ω indicated by a solid black contour), as quantified by $O_2 \times \mathcal{V}_\Omega^\downarrow$ normalized by the volume of Ω , in the preindustrial state. (c–d) As (a–b) for Ω the deep ETP. (e–h) As (a–d) for $\Delta(O_2^{\text{pre}} \times \mathcal{V}_\Omega^\downarrow)$ for the RCP4.5 perpetual 2090s. (i–l) As (e–h) for RCP8.5. Note the nonlinear color scale and that the contributions plotted are per unit horizontal area.

608 For the upper ETP, the origin of preformed oxygen in the preindustrial state (Fig. 9a)
 609 shows that while much oxygen comes from the overlying surface, a considerable fraction
 610 is supplied from Mode and Intermediate water-formation regions in the Pacific, and from
 611 deep-water formation regions in the Southern Ocean (Weddell and Ross Seas) and North
 612 Atlantic. For the deep ETP in the preindustrial state, the tropical and subtropical con-
 613 tributions are much weaker while contributions from the deep-water formation regions
 614 of the Southern Ocean and the North Atlantic are more important.

615 For the perpetual-2090s states, the largest decreases in preformed oxygen origin
 616 occur in the deep-water formation regions, particularly near the Weddell and Ross Seas.
 617 The supply of O_2^{pre} from south of 60°S declines by about 70 % and 50 % for the upper
 618 and deep ETP, respectively, for the RCP4.5 scenario, and almost completely shuts down
 619 for both the upper and deep ETP for RCP8.5. As discussed for Fig. 6 and underscored
 620 by the similarity between Fig. 9 and Appendix Fig. B4, this is dominantly due to circulation-
 621 driven changes in ventilation. Large-scale increases of the O_2^{pre} supply are most promi-
 622 nent in the subtropical gyres, which are more important oxygen sources for the ETP in
 623 our perpetual-2090s states.

624 4 Discussion

625 We investigated the deoxygenation of the ocean for idealized steady-state biogeo-
 626 chemistry in equilibrium with frozen-in-time physical ocean states. We used two ocean
 627 states averaged over the 2090s for the RCP4.5 and RCP8.5 scenarios, held constant in
 628 time for perpetuity, and a corresponding 1990s steady state (“preindustrial” for short)
 629 for our analysis. To attribute the deoxygenation to its drivers, we focused on the east-
 630 ern tropical basins (primarily the Pacific) as these contain OMZs in the current ocean,
 631 and because their deoxygenation is typical of the large-scale steady-state response in our
 632 model. The key driving mechanisms were quantified by decomposing the oxygen changes
 633 into contributions from changes in surface solubility, ocean circulation, and oxygen uti-
 634 lization rates. Here we discuss caveats of our approach and compare our results to other
 635 work on ocean deoxygenation.

636 **4.1 Caveats**

637 A number of caveats must be kept in mind when interpreting our findings. Some
 638 caveats also apply to the nutrient and carbon cycles and have been previously discussed
 639 by Pasquier, Holzer, Chamberlain, Matear, et al. (2023) and Pasquier, Holzer, and Cham-
 640 berlain (2023). Below we detail the caveats specific to our analysis of deoxygenation.

641 (i) The biogeochemical states analyzed here are steady and embedded in circulations that
 642 are frozen in time. By contrast, the real ocean circulation is currently slowing down and
 643 will continue to evolve for millennia even for fixed external forcing (e.g., Srokosz & Bry-
 644 den, 2015). Given the ocean's wide range of transit times (e.g., Primeau, 2005), the cir-
 645 culation will keep changing well beyond the 21st century until deep convection, venti-
 646 lation, and overturning eventually recover after a few millennia (e.g., Schmittner et al.,
 647 2008), which results in a different state from those considered here. Thus, neither the
 648 oxygen distribution nor the circulation and thermodynamic ocean state are expected to
 649 be anywhere near steady by the end of the 21st century (e.g., Shaffer et al., 2009). Our
 650 biogeochemical states can therefore not be interpreted as predictions of the 21st century.
 651 In particular, by allowing oxygen to fully equilibrate with frozen circulations that have
 652 strongly weakened Southern Ocean ventilation and bottom-water formation, our ideal-
 653 ized steady states exhibit intense abyssal deoxygenation that will certainly not have man-
 654 ifested by 2100. However, our analysis does provide a glimpse into the possible mech-
 655 anisms that could shape the oxygen response on its very longest timescales. Furthermore,
 656 our steady-state framework does not account for natural variability, and in particular
 657 does not account for seasonal variations. We therefore cannot capture the effects from
 658 seasonally covarying changes in biology, physics, and thermodynamics, which play a sig-
 659 nificant role in the seasonality of oxygen in the upper few hundred meters as seen in both
 660 observations and models (see, e.g., Jin et al., 2007; Graco et al., 2017; Espinoza-Morriberón
 661 et al., 2021; Pitcher et al., 2021, to cite a few).

662 (ii) Our quantitative results are specific to the circulation of the parent climate model.
 663 The unrealistically deep Southern Ocean mixed layer of the preindustrial state inherited
 664 from the parent ACCESS1.3 model (Bi et al., 2013), and its shoaling in the future, leave
 665 a pronounced imprint on our results. However, unrealistically deep mixed layers in the
 666 polar Southern Ocean are a feature common to virtually all CMIP5 models (e.g., de Lavergne
 667 et al., 2014), in which AABW is formed by deep convection compensating for unresolved

sinking of Antarctic shelf waters. Importantly, the deoxygenation drivers identified here
 are unlikely to depend on which particular CMIP5 model is used, given that most of them
 share the qualitative feature of declining Southern Ocean ventilation and shoaled mixed
 layers at the end of the 21st century (e.g., de Lavergne et al., 2014; Heuzé et al., 2015;
 Kwiatkowski et al., 2020). These are both critical circulation changes for producing the
 equilibrated intense deoxygenation when the circulation is frozen in time. In addition,
 the ACCESS1.3 parent model does not include melting land-fast ice sheets, which im-
 pact Southern Ocean ventilation (Li et al., 2023; Chen et al., 2023). If meltwater from
 ice sheets were included, we would expect a stronger reduction in Southern Ocean ven-
 tilation (Purich et al., 2018; Purich & England, 2023), which we would expect to strengthen
 the circulation-change contribution to deoxygenation. We emphasize, however, that ac-
 curate flow changes with detailed realism are not important to our idealized scenarios.
 Any circulation with reduced Southern Ocean ventilation and bottom-water formation
 that is frozen in time is likely to produce intense abyssal deoxygenation similar to what
 we document here.

(iii) In quantitative detail, our results are also specific to the biogeochemistry model em-
 ployed (PCO2; Pasquier, Holzer, Chamberlain, Matear, et al., 2023), which was designed
 to be relatively simple and does not explicitly represent every mechanism at play in the
 real ocean. Potentially important missing mechanisms include feedbacks from the nitro-
 gen cycle, which are linked to oxygen through denitrification and nitrification. Denitri-
 fication, which is only modelled implicitly in PCO2 (see Methods, Eq. (1)), is important
 because anaerobic respiration in low oxygen environments acts as an effective oxygen source.
 Conversely, nitrogen fixation and nitrification, which produce nitrite and nitrate by con-
 suming oxygen, are not represented at all in PCO2. Effects from the nitrification–denitrification
 imbalance on the oxygen cycle, expected to contribute about two thirds of a ~6 % in-
 crease in the global O₂ inventory by the year 8000 (Oschlies et al., 2019), are therefore
 not captured in our model. However, we note that this imbalance is expected to be dom-
 inated by denitrification (which *is* parameterized in PCO2) and remains secondary for
 the first few centuries of sluggish circulation until about the year 5000 when the over-
 turning circulation recovers.

4.2 Relation to previous work

Because our analysis is framed for steady-state biogeochemistry in equilibrium with frozen-in-time circulations, we do not expect a detailed match with previous studies based on transient simulations. We do, however, expect similarities with simulations that last long enough for the effect from slow processes to manifest. In particular, this includes processes mediated by the slowdown of the deep ocean circulation, which is the dominant driver of deoxygenation in our analyses and operates on multi-centennial timescales (e.g., Primeau, 2005), with effects that will not have asserted themselves by the end of the 21st century in transient simulations of oxygen (e.g., Moore et al., 2018). However, the relatively more sluggish ocean state predicted for the next few centuries will likely only be temporary. A more vigorous circulation is expected to return after several millennia as deep ocean temperatures equilibrate (e.g., Schmittner et al., 2008; Frölicher et al., 2020). The more vigorous circulation and stronger Southern Ocean ventilation predicted for a future steady state of the ocean could thus result in the opposite response found here for our perpetually warmer and slower ocean states. In particular, in the very long term, deep preformed O₂ could actually increase despite a globally warmer ocean because of a poleward shift in the origin of deep oxygen. We therefore expect our results to be closest to predictions for a few centuries into the future before a more vigorous circulation re-establishes. We also note that differences in biogeochemistry, in ocean circulation, in scenarios and forcings, and so on, further complicate quantitative comparisons.

The very intense deoxygenation seen here at depth is driven by circulation changes that act in perpetuity, while corresponding effects in transient simulations have not fully developed by 2100. Thus, while our results agree qualitatively with predictions for the end of the 21st century, they differ in magnitude, especially in the deep ocean. For the upper ocean, Kwiatkowski et al. (2020) reported a (10±2)% decline in 100–600 m deep oxygen across CMIP5 models and a (13±5)% decline across CMIP6 models for RCP8.5 and SSP5-8.5, respectively, compared to the ~20% decline for our RCP8.5-based perpetual-2090s steady state. (CMIP6 uses the “Shared Socioeconomic Pathway” (SSP) classification (Riahi et al., 2017) where SSP5-8.5 nominally matches RCP8.5 (Arias et al., 2021).) Similarly, for RCP4.5, Kwiatkowski et al. (2020) reported a 6±3% decline for CMIP5 and a 8±4% decline for CMIP6, compared to a ~7% decline in this study for the same scenario. Near the sea floor, Kwiatkowski et al. (2020) reported a weak but consistent 6±2% oxygen decline across CMIP6 models and scenarios, compared to a much stronger

732 ~40 % and ~80 % decline in the abyss of our RCP4.5- and RCP8.5-based states, respec-
 733 tively. The volumes of hypoxic regions in our perpetual-2090s states thus are dramat-
 734 ically larger than the future predictions of a moderate ~10 % expansion in mild hypoxia
 735 and a contraction of the OMZ core (e.g., Gnanadesikan et al., 2012; Busecke et al., 2022).

736 Longer-term transient simulations in principle allow for closer comparisons with
 737 our steady-state biogeochemistry embedded in frozen-in-time circulations but the recov-
 738 ery of the transient ocean circulation intervenes before the long-term effects of circula-
 739 tion slowdown can fully develop. Running a climate model with $p\text{CO}_2$ at three times its
 740 preindustrial level from 2100 onward, Matear and Hirst (2003) reported a ~30 % decline
 741 in O_2 below 4000 m by 2700. This O_2 decline is larger than those estimated for 2100 but
 742 still far from the corresponding 80 % decline of our RCP8.5 perpetual-2090s state, be-
 743 cause the circulation effects on O_2 are not fully developed as evidenced by a deep O_2 trend
 744 that remains strongly negative by 2700. Matear and Hirst (2003) report spatial patterns
 745 that are similar to our steady-state responses, with intense O_2 declines in the deep South-
 746 ern Ocean driven by decreased ventilation. However, the simulation by Matear and Hirst
 747 (2003) was not continued beyond 2700, which is roughly when the circulation is expected
 748 to start recovering. In a multimillennial double- $p\text{CO}_2$ simulation, Frölicher et al. (2020)
 749 find a 700-yr decline in O_2 mostly below 2000 m accumulating to a ~10 % loss globally
 750 (compared to 40 % for our RCP4.5 perpetual-2090s state) before O_2 slowly increases again
 751 over multiple millennia driven by the recovery of Southern-Ocean ventilation. In another
 752 multimillennial simulation with $p\text{CO}_2$ reaching almost 2000 μatm around year 2300 and
 753 slowly declining to ~1200 μatm over the next five millennia, Oschlies et al. (2019) find
 754 an O_2 decline of ~25 %, also reached around year 2700, before O_2 levels increase again
 755 with the recovering circulation.

756 Our analyses differ from previous studies in attributing deoxygenation to specific
 757 mechanisms. In our work here, solubility alone accounts for less than 10 % of the global
 758 O_2 decline, which is lower than previous estimates. However, despite some consensus,
 759 previous studies likely overestimate the solubility contribution. Studies that infer the sol-
 760 ubility contribution from a residual, typically between a climate-change simulation and
 761 a similar simulation with the solubility fixed to preindustrial values (e.g., Matear & Hirst,
 762 2003), unintentionally include effects from changes in ventilation patterns (which should
 763 be attributed to circulation change) because the residual includes spatial correlation (“cross”)
 764 terms, which we estimate to be order 20 % for our steady states in frozen-in-time circu-

765 lations. Approximations based on heat flux generally overestimate the contribution from
766 solubility changes because they assume complete saturation (e.g., 20 %–30 %; Bopp et
767 al., 2002; Palter & Trossman, 2018). Solubility-change contributions quantified through
768 an abiotic/preformed O₂ tracer are generally overestimated yet more (e.g., 30 %–50 %;
769 Oschlies et al., 2019; Oschlies, 2021) because the preformed tracers respond to both sat-
770 uration and circulation changes. Similarly, solubility contributions quantified directly by
771 the change in saturation concentration as a function of in situ temperature and salin-
772 ity are overestimated even more (e.g., 40 %–70 %; Frölicher et al., 2020). Only studies
773 that perturb surface solubility alone, e.g., by prescribing the future surface temperature
774 for the solubility in an otherwise unperturbed preindustrial state, can provide unbiased
775 estimates. This includes, e.g., the 15 %, 25 %, and 35 % estimates by Matear et al. (2000),
776 Bopp et al. (2002), and Plattner et al. (2001), respectively (the differences likely stem-
777 ming from model-specific biases, with higher estimates corresponding to states with smaller
778 changes in Southern-Ocean ventilation.) Given these overestimates of solubility-change
779 contributions to the ocean oxygen inventory, and given that spatial correlations between
780 changes in ventilation patterns and solubility are typically overlooked, it is likely that
781 previous studies have typically underestimated the effects from circulation changes.

782 5 Conclusions

783 We quantified the drivers of large-scale ocean deoxygenation for idealized steady-
784 state biogeochemistry embedded in perpetual-2090s ocean states based on RCP4.5 and
785 RCP8.5 ACCESS1.3 simulations. Our analysis is idealized because we allowed oxygen
786 to fully equilibrate with a perpetually warmer and slower ocean, which is in stark con-
787 trast to transiently evolving biogeochemistry embedded in a more realistic dynamically
788 changing circulation. Changes in biogeochemistry were evaluated relative to a steady prein-
789 dustrial state and analyzed for the eastern tropical Pacific (ETP), which contains the
790 largest hypoxic volume. We partitioned changes in TOU and preformed oxygen into their
791 drivers, i.e., into contributions from changes in circulation, respiration, solubility, and
792 their interactions (cross terms).

793 Our quantification of the deoxygenation drivers for specific ocean regions employed
794 novel diagnostic methods that leveraged the steady-state nature of our idealized biogeo-
795 chemical states. Key to our being able to isolate — for the first time — the role of cir-
796 culation changes in driving deoxygenation is the conceptually novel upstream exposure

time, a circulation timescale that controls the oxygen deficit of a given subvolume Ω of the ocean. Specifically, it is the time for which the oxygen that is “missing” from Ω was exposed to upstream respiration. The upstream exposure time thus provides the precise connection between TOU and OUR (Holzer, 2022) and, as shown here, the precise link between ventilation volume and preformed oxygen. In essence, the upstream exposure time, which is determined by the circulation only, traces TOU and preformed oxygen back in time to their origin.

Our main conclusions are as follows:

1. Keeping the 2090s ocean state frozen in time leads to steady-state oxygen distributions characterized by intense global-scale deoxygenation at depth. Global oxygen inventories decline by 30 % and 60 % for the RCP4.5 and RCP8.5 scenarios, respectively. For the extreme RCP8.5 case, Pacific abyssal waters become severely hypoxic ($pO_2 \leq 15 \mu\text{M}$) over the entire basin, while Atlantic and Indian Ocean abyssal waters become mildly hypoxic ($pO_2 \leq 100 \mu\text{M}$) everywhere. The extent of hypoxic regions in the upper ocean changes remarkably little in our more poorly ventilated perpetual-2090s states, owing to decreased preformed oxygen being compensated by reduced TOU.
2. For our idealized steady states, intense abyssal TOU increases are dominantly driven by the perpetual 2090s circulation being slower, thus allowing respiration to act over longer times while modest upper-ocean TOU decreases are characterized by close compensation between respiration-only and circulation-only effects. Specifically, in the deep ETP, TOU increases of 50 % for RCP4.5 and 100 % for RCP8.5 are driven by 2–3 times longer upstream exposure to respiration, which overwhelms the decline in respiration rates. In the upper ETP, TOU decreases by about 10 %. Thus, despite the global decline in respiration rates, the permanently slower circulation of our idealized states drives intense deoxygenation at depth and prevents increased oxygenation in the upper ocean.
3. In our idealized perpetual-2090s states, preformed oxygen declines virtually everywhere driven mostly by shifts in ventilation patterns, rather than by the decrease in solubility due to warmer sea-surface temperatures. More than 70 % of the decline in preformed oxygen is driven by its surface origin shifting away from high latitudes toward lower latitudes, where warmer waters hold less oxygen. In

829 situ warming-driven solubility reductions by themselves, at fixed circulation, re-
830 duce preformed oxygen by only $\sim 30\%$ in the upper ETP and by less than 20%
831 in the deep ETP, accounting for less than 10% of the overall deoxygenation. Thus,
832 while preformed oxygen is often thought to decrease because of warming-driven
833 reduced solubility (e.g., Palter & Trossman, 2018; Oschlies et al., 2019; Couespel
834 et al., 2019; Oschlies, 2021), our analysis reveals that, at least when the 2090s ocean
835 state is maintained in perpetuity, the change in ventilation pathways is the dom-
836 inant driver.

837 Our results show that, for our idealized states, circulation change is the key driver of de-
838 oxygenation. However, it remains an open question what the precise contribution of cir-
839 culation change will be in the future ocean. Our analysis suggests that to understand
840 the fate of oxygen in the ocean, it is important to carefully quantify ventilation patterns
841 and key ocean circulation timescales. Of particular importance is the upstream expo-
842 sure time which is a key control on both preformed oxygen and TOU. For steady state,
843 the necessary computations can efficiently be performed by building and using the as-
844 sociated transport matrices as was done here, and which we hope will become a more
845 widely adopted practice. For transient states, the analysis becomes significantly more
846 complex, and extending our work to a dynamically changing oxygen cycle is left to the
847 future.

848 **Appendix A Model–observations comparisons**

849 Figure A1 shows the basin zonal-mean pO_2 for the preindustrial state of our model
 850 and for the GLODAPv2 observations, along with the corresponding mismatch. The un-
 851 realistically deep mixed layers of the Southern Ocean in the parent model manifest as
 852 overestimated pO_2 in the Atlantic and Pacific south of 60°S. Other systematic model bi-
 853 ases are visible, for example in the northern Indian Ocean, where PCO2 overestimates
 854 pO_2 , and in the tropical and subtropical upper Atlantic and Pacific, where PCO2 un-
 855 derestimates pO_2 .

856 Figure A2 shows the areal extent of each hypoxia category in each ocean basin as
 857 modelled for the preindustrial state and as captured by the GLODAPv2 observations.
 858 The extent of the Atlantic and Pacific hypoxic areas is generally overestimated, while
 859 the extent of the Indian-Ocean hypoxic areas is generally underestimated particularly
 860 at depth, consistent with Fig. A1. We note that the pO_2 thresholds used are different
 861 for model and observations as they were adjusted for the model so that the global hy-
 862 poxic volume for a given category is the same for the model as for GLODAPv2 (Meth-
 863 ods, Section 2.6). (Note that the global match does not guarantee matching volumes within
 864 a given basin.)

865 Figure A3 shows the geographic distribution of hypoxic waters as quantified by the
 866 water-column minimum of pO_2 for the preindustrial model state and for the GLODAPv2
 867 observations. While the large-scale patterns seen in the observations are captured by the
 868 model, there are significant mismatches. The underestimated pO_2 in the Pacific and At-
 869 lantic manifest as OMZs (hypoxia category C) that are larger than observed. The model
 870 places the Indian Ocean OMZ southeast of western Indonesia while observations show
 871 it to occur in the Bay of Bengal and in the Arabian Sea.

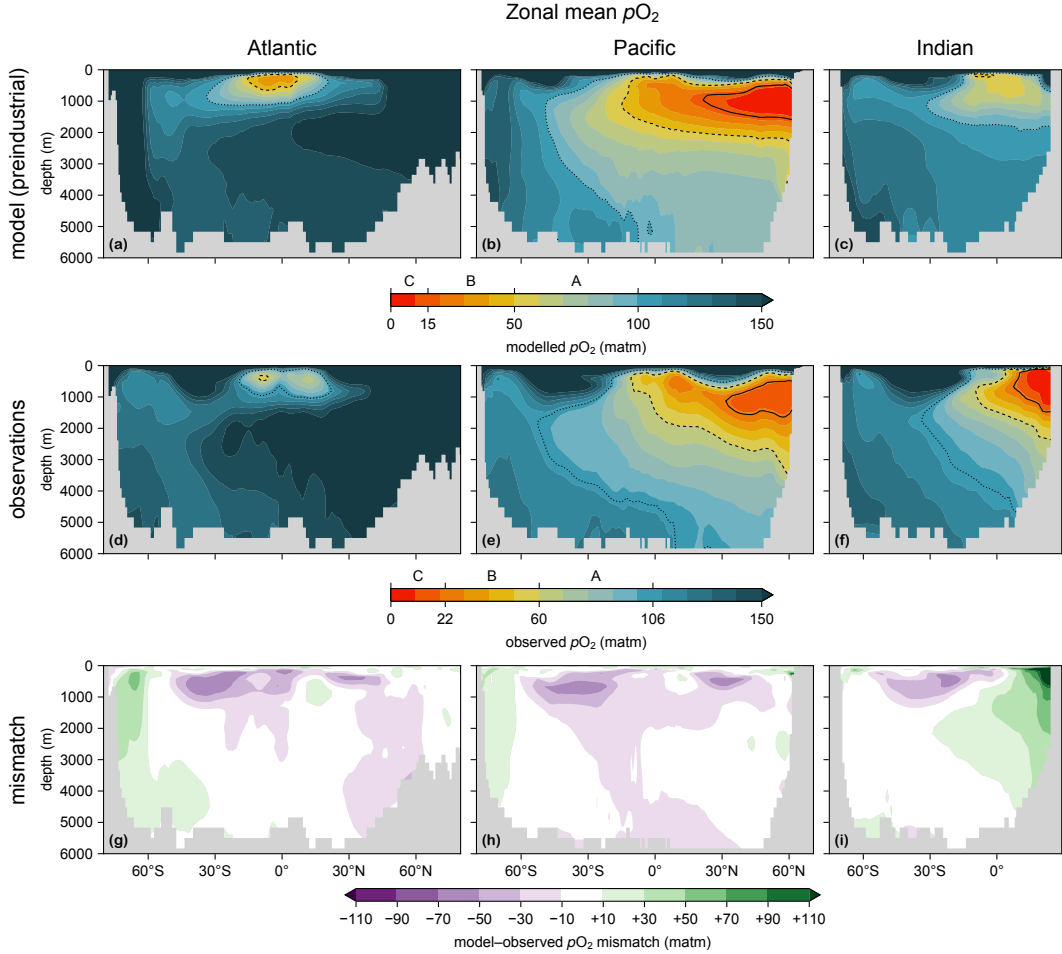


Figure A1. (a) Atlantic, (b) Pacific, and (c) Indian Ocean zonal mean $p\text{O}_2$ for the preindustrial state. The dotted, dashed, and solid contour lines indicate the thresholds of hypoxia categories A, B, and C, respectively (which are different for model and observations; see Methods, Section 2.6). (d–f) As (a–c) for observations. (g–i) As (a–c) for the model–observations mismatch. The Atlantic basin excludes the Gulf of Mexico and the Caribbean, and the Pacific basin excludes the Sea of Japan so that the zonal means are more cleanly interpretable.

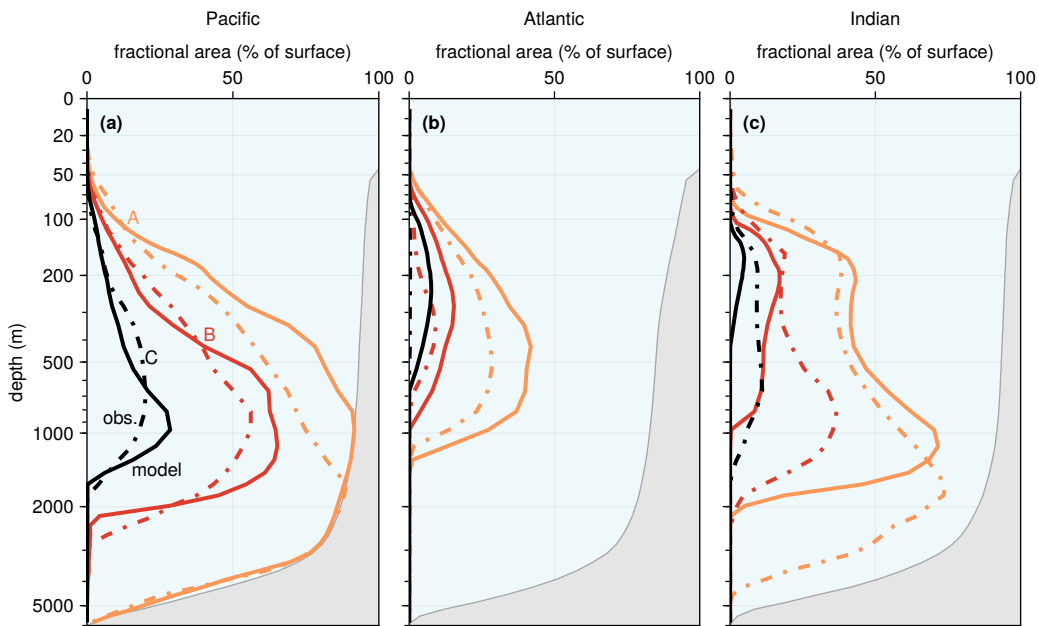


Figure A2. (a) Pacific depth profiles of the spatial extent of mild (A, orange), intermediate (B, red), and severe hypoxia (C, black) for the modelled preindustrial state (model; solid lines) and the observations (obs.; dash-dotted lines). (b) As (a) for the Atlantic. (c) As (a) for the Indian Ocean. (The gray shading represents the seafloor.) Note the nonlinear depth scale and that the $p\text{O}_2$ thresholds used for model and observations are different (see Methods, Section 2.6).

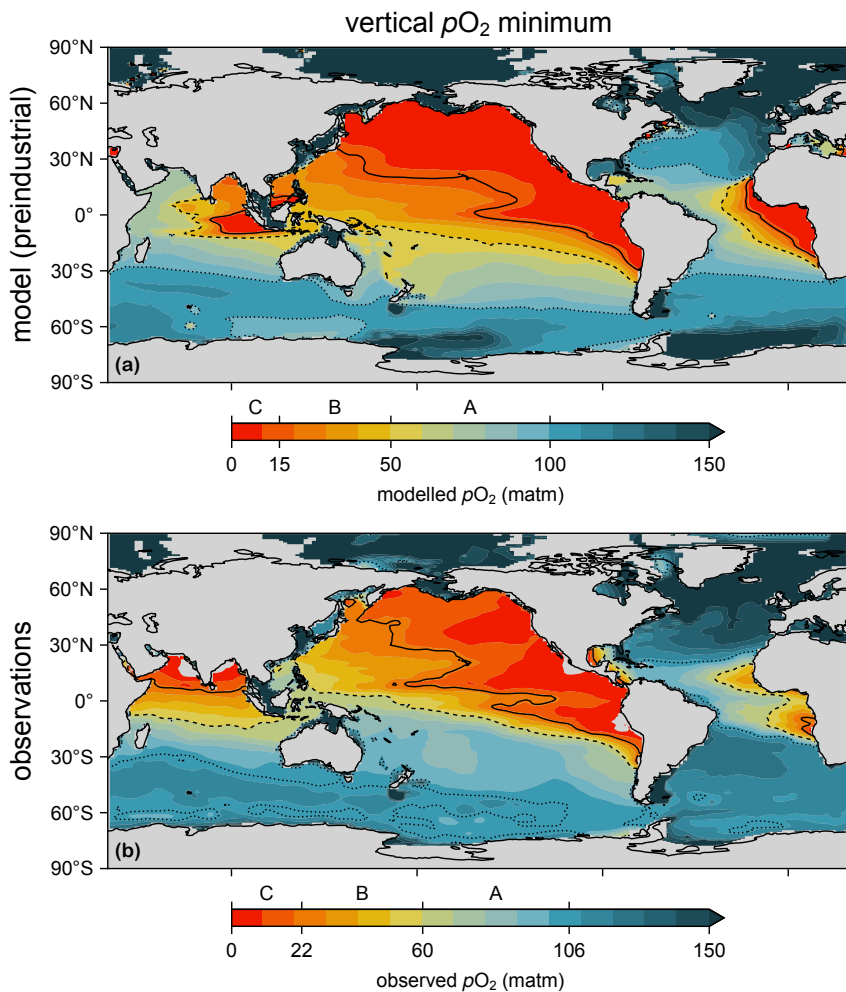


Figure A3. (a–b) Maps of the water-column minimum $p\text{O}_2$ for (a) the modelled preindustrial state and (b) observations. The dotted, dashed, and solid contour lines indicate the thresholds of hypoxia categories A, B, and C, respectively (which are different for model and observations; see Methods, Section 2.6).

872 **Appendix B TOU and O_2^{pre} : patterns and drivers**

873 The left plots of Fig. B1 show the Pacific zonal mean O_2^{pre} for the preindustrial state
 874 and the corresponding changes for the perpetual-2090s states. Near the surface, O_2^{pre} is
 875 higher in cold waters with greater oxygen solubility, and in the interior O_2 traces out (wa-
 876 ter) ventilation pathways. In the perpetual-2090s states, preformed O_2 declines almost
 877 everywhere and more strongly at depth, except in the surface Southern Ocean above ~ 200 m.

878 The right plots of Fig. B1 show zonal mean TOU, which increases progressively as
 879 water traverses sinking organic matter where respiration strips out oxygen. TOU is gen-
 880 erally largest at depths of about 500–1500 m in the preindustrial state, and increases sig-
 881 nificantly at depth in the perpetual-2090s states. TOU and its changes are governed by
 882 both oxygen utilization rates (OUR) and upstream sweeping times, shown below.

883 OUR, shown in the left plots of Fig. B2, is generally surface intensified by several
 884 orders of magnitude as OUR is tightly linked to nutrient and carbon remineralization
 885 which attenuates quickly with depth. In our perpetual-2090s states, biological produc-
 886 tion and OUR decline globally though they are some local increases, mostly owing to spa-
 887 tial shifts in the nutrient supply. However, the effect of changes in OUR on O_2 is mod-
 888 ulated by the time over which oxygen is exposed to respiration, discussed next.

889 The zonal-mean upstream exposure time $\Gamma_\Omega^\uparrow(\mathbf{r})$ is shown in Fig. B2 for the case where
 890 the interior volume Ω of interest is either the upper ETP (middle plots) or deep ETP
 891 (right plots). Because in steady state the upstream exposure time is also $\Gamma_\Omega^\uparrow(\mathbf{r})$, the time
 892 that water at \mathbf{r} will spend in Ω , its magnitude approximately scales with the volume of
 893 Ω . Furthermore, because the deep circulation is much more sluggish than in the wind-
 894 driven thermocline, upstream exposure times are shorter for the upper ETP (less than
 895 ~ 20 years) than for the deep ETP (up to ~ 450 years). Γ_Ω^\uparrow is generally larger close to
 896 Ω and decreases with distance from Ω . Qualitatively, Γ_Ω^\uparrow can be thought of as path se-
 897 lector roughly akin to the concentration of fluid elements destined to pass through Ω be-
 898 fore exposure to the euphotic zone. Thus, Γ_Ω^\uparrow is shorter further away from Ω because more
 899 of the water there will be reexposed to the euphotic zone before it has a chance to pass
 900 through Ω .

901 In the perpetual-2090s states, a slower circulation tends to increase Γ_Ω^\uparrow , but altered
 902 ventilation pathways can also reduce Γ_Ω^\uparrow (lower middle and right plots of Fig. B2). For

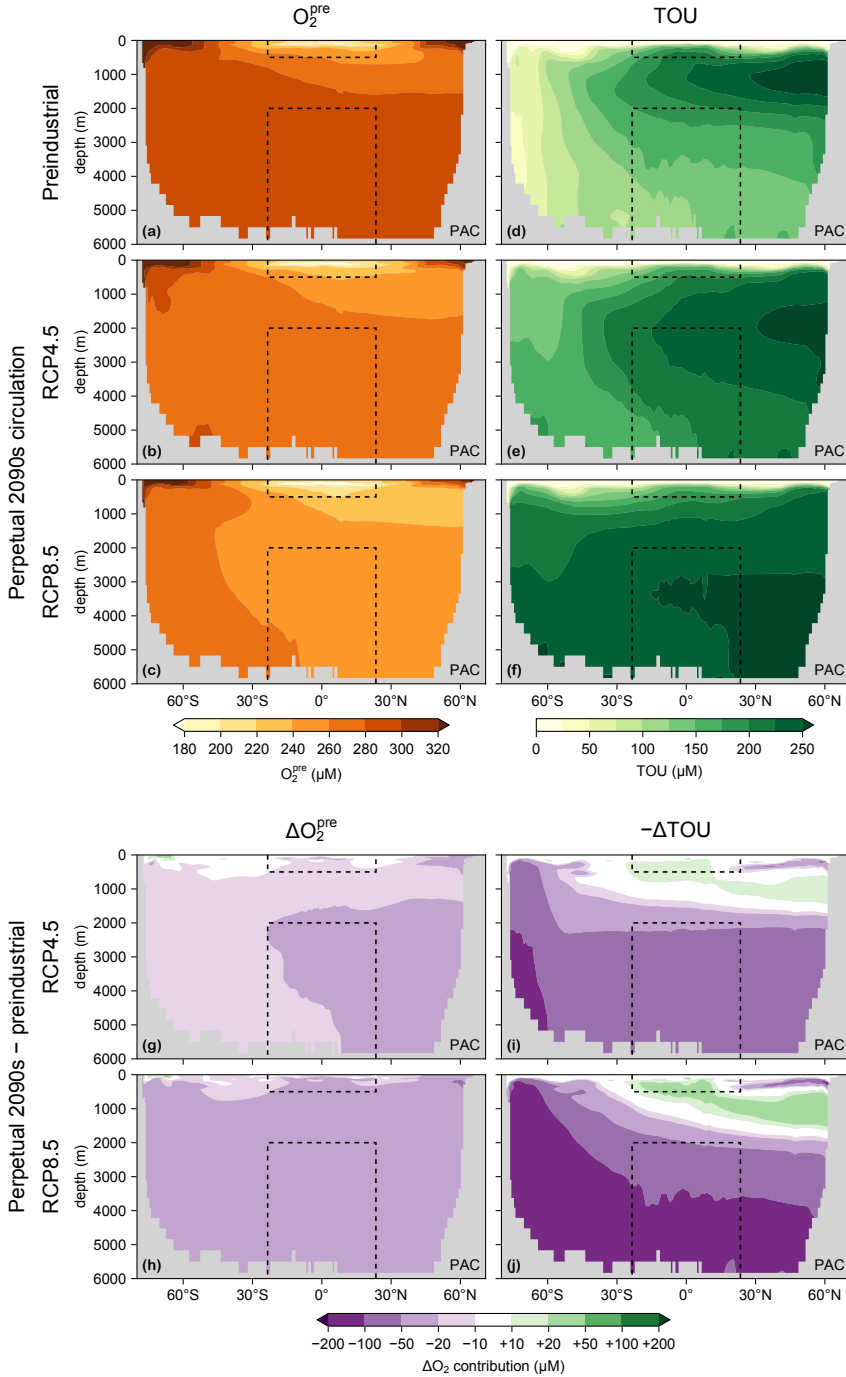


Figure B1. (a) Pacific zonal mean O_2^{pre} for the preindustrial state. (b–c) As (a) for the perpetual-2090s states (based on RCP4.5 and RCP8.5). (d–f) As (a–c) for TOU. (g–j) ΔO_2^{pre} and ΔTOU for RCP4.5 and RCP8.5. Dashed lines indicate the upper and deep ETP regions. Note the nonlinear color scale and that the Sea of Japan has been excluded so that these zonal means are more cleanly interpretable.

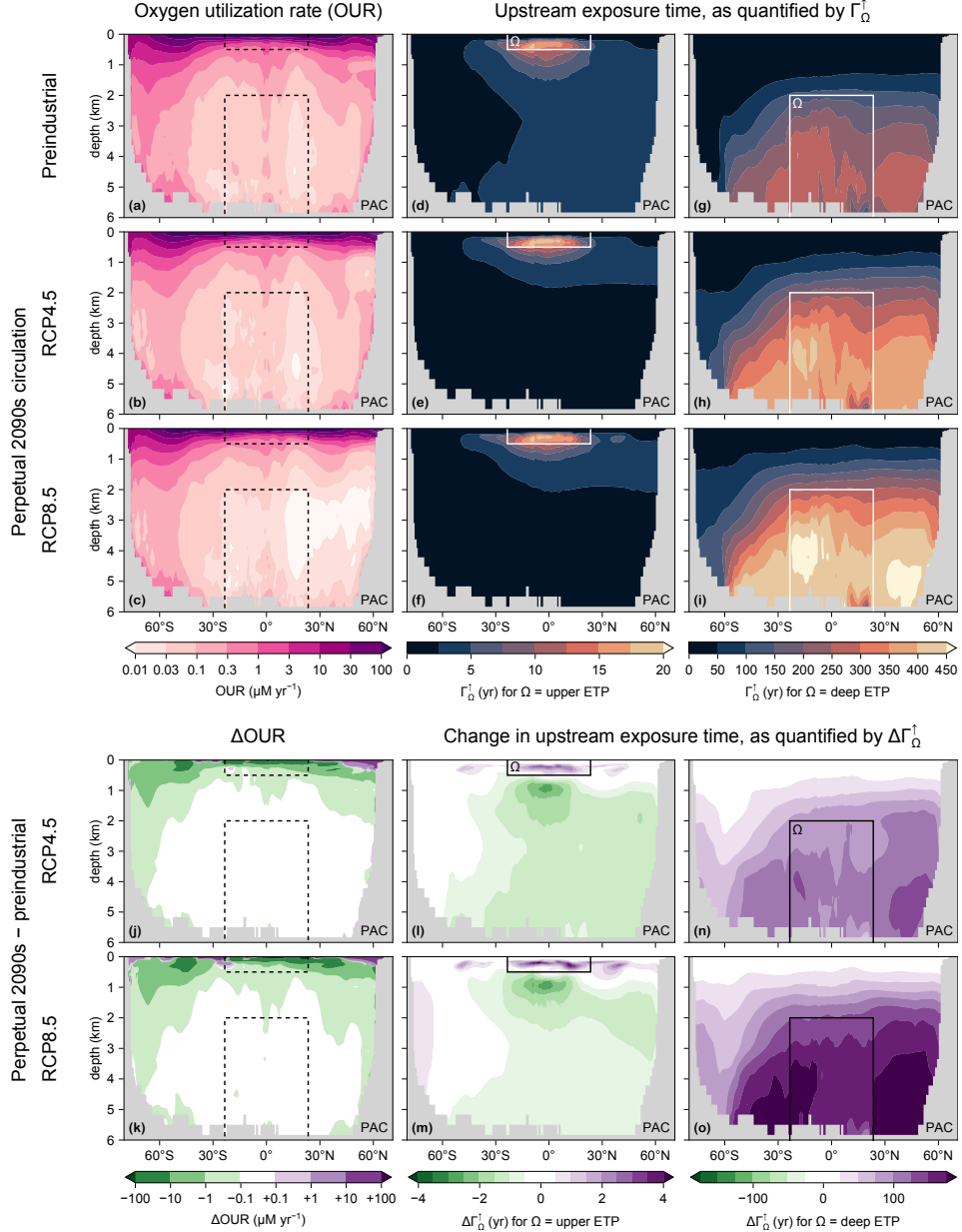


Figure B2. (a) Pacific zonal mean OUR for the preindustrial state. Dashed lines indicate the upper and deep ETP regions (Ω 's). (b–c) As (a) for the perpetual-2090s states (RCP4.5 and RCP8.5). (d–f) As (a–c) for the upstream exposure time Γ_Ω^\uparrow of the upper ETP (above 500 m; solid white line). (g–i) As (d–f) for the deep ETP (below 2000 m). (j–k) As (b–c) for ΔOUR . (l,m,n,o) As (e,f,h,i) for $\Delta\Gamma_\Omega^\uparrow$. Note the nonlinear color scales and that the Sea of Japan has been excluded so that these zonal means are more cleanly interpretable.

the deep ETP, the circulation slowdown drives strong Γ_Ω^\uparrow increases throughout the deep Pacific north of the Southern Ocean. By contrast, for the upper ETP, Γ_Ω^\uparrow increases above

500 m, but decreases in the Pacific below the thermocline north of $\sim 30^{\circ}\text{S}$. These decreases are likely because the surface ocean becomes more isolated in our perpetual-2090s states (Pasquier, Holzer, & Chamberlain, 2023), reducing the flow of mid-depth, low-latitude waters through the upper ETP on their way back to the surface. Conversely, slight increases in $\Gamma_{\Omega}^{\uparrow}$ in the deep polar Southern Ocean for RCP8.5 are likely due to deep Southern Ocean waters preferentially upwelling at lower latitudes instead of being quickly mixed back to the Southern Ocean euphotic zone.

Changes in O_2^{pre} are driven by changes in euphotic O_2 and by changes in ventilation patterns. Fig. B3 shows maps of the changes in euphotic-mean oxygen concentrations. Except at high latitudes, declines are widespread and attributable to warming-driven solubility reductions. Increases can be caused by decreased temperatures (e.g., in the North Atlantic cold blob) but the most intense increases occur near the Weddell and Ross Seas due to reduced vertical mixing, which allows for better air-sea oxygen equilibration as discussed in Section 3.2 of the main text. However, solubility changes are not the dominant driver of reduced interior O_2^{pre} concentrations.

Decreases in the O_2^{pre} inventory of an interior subvolume Ω are dominantly driven by changes in ventilation patterns (Section 3.2), as quantified by the amount of the Ω volume ventilated per unit area, $\mathcal{V}_{\Omega}^{\downarrow}$. Maps of $\mathcal{V}_{\Omega}^{\downarrow}$ for Ω being the upper and deep ETP are plotted in Fig. B4 for the preindustrial state, along with the changes for our perpetual-2090s states. The patterns of $\mathcal{V}_{\Omega}^{\downarrow}$ strongly mirror those of $\text{O}_2 \mathcal{V}_{\Omega}^{\downarrow}$ in Fig. 9 of the main text. While $\sim 40\%$ of the upper ETP is ventilated from directly above, the remaining $\sim 60\%$ is ventilated from distant regions, with subtropical and subpolar contributions in the Pacific, as well as contributions from the North Atlantic, the Ross Sea, and the Weddell Sea. By contrast, the bulk of the deep ETP is ventilated from distant regions, with only about 1% from directly above. In our perpetual-2090s states, the subpolar and Southern Ocean contributions generally decline in favor of subtropical and tropical contributions, effectively shifting the origin of preformed O_2 equatorward where warmer waters hold less dissolved oxygen.

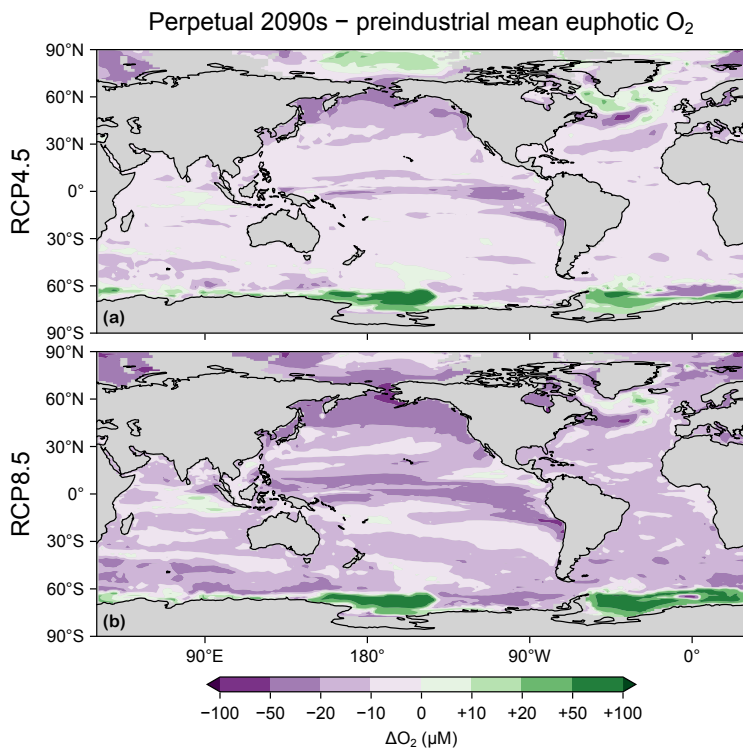


Figure B3. (a) Change in the euphotic-mean O_2 between the preindustrial state and the perpetual-2090s state for the RCP4.5 scenario. (b) As (a) for RCP8.5. Note the nonlinear color scale.

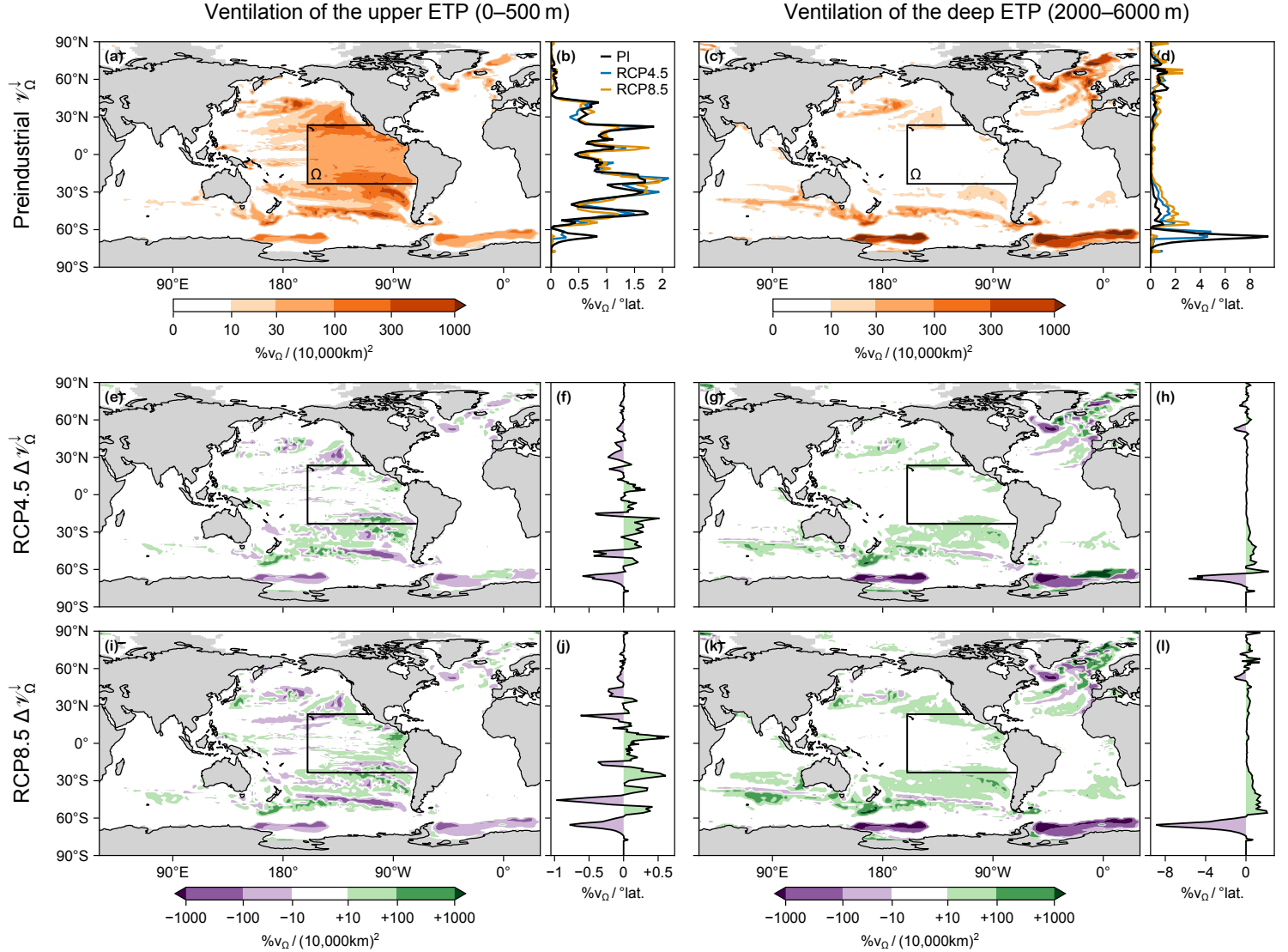


Figure B4. (a) Map and (b) zonal integral of the fractional Ω volume ventilated from the surface for Ω being the upper ETP (solid black contour), as quantified by $\mathcal{V}_\Omega^\downarrow$, in the preindustrial state. (c–d) As (a–b) for Ω being the deep ETP. (e–h) As (a–d) for $\Delta\mathcal{V}_\Omega^\downarrow$ in the RCP4.5 scenario. (i–l) As (e–h) in the RCP8.5 scenario. Note the nonlinear color scales.

933 **Appendix C Open Research**

934 The MATLAB and Julia code corresponding to this work will be made available
 935 upon acceptance of this article. The figures were created in Julia (Bezanson et al., 2017)
 936 with the Makie.jl plotting package (Danisch & Krumbiegel, 2021). The transport ma-
 937 trices were built from the historical, RCP4.5, and RCP8.5 ACCESS1.3 CMIP5 model
 938 runs available at <https://esgf.nci.org.au/projects/esgf-nci/>. This output also
 939 includes temperature, salinity, photosynthetically available radiation (PAR), sea-ice, and
 940 wind fields.

941 **Acknowledgments**

942 This work was supported by Australian Research Council grant DP210101650 (to
 943 MH) and undertaken with the assistance of resources and services from the National Com-
 944 putational Infrastructure (NCI), which is supported by the Australian Government. NLB
 945 support for this project received grant funding from the Australian Government as part
 946 of the Antarctic Science Collaboration Initiative program.

947 **References**

- 948 Arias, P., Bellouin, N., Coppola, E., Jones, R., Krinner, G., Marotzke, J., ... Zickfeld,
 949 K. (2021). Technical summary [Book Section]. In V. Masson-Delmotte et
 950 al. (Eds.), *Climate change 2021: The physical science basis. contribution of
 951 working group i to the sixth assessment report of the intergovernmental panel
 952 on climate change* (pp. 33–144). Cambridge, United Kingdom and New York,
 953 NY, USA: Cambridge University Press. doi: 10.1017/9781009157896.002
- 954 Bao, Y., & Li, Y. (2016, December). Simulations of dissolved oxygen concentration
 955 in CMIP5 Earth system models. *Acta Oceanologica Sinica*, 35(12), 28–37. doi:
 956 10.1007/s13131-016-0959-x
- 957 Beman, J. M., & Carolan, M. T. (2013). Deoxygenation alters bacterial diversity
 958 and community composition in the ocean’s largest oxygen minimum zone. *Na-
 959 ture Communications*, 4(1), 2705. doi: 10.1038/ncomms3705
- 960 Bezanson, J., Edelman, A., Karpinski, S., & Shah, V. B. (2017). Julia: A fresh ap-
 961 proach to numerical computing. *SIAM Review*, 59(1), 65–98. doi: 10.1137/
 962 141000671

- 963 Bi, D., Marsland, S. J., Uotila, P., O'Farrell, S., Fiedler, R. A. S., Sullivan, A., ...
 964 Hirst, A. C. (2013). ACCESS-OM: the ocean and sea ice core of the ACCESS
 965 coupled model. *Australian Meteorological and Oceanographic Journal*, 63,
 966 213-232.
- 967 Bindoff, N. L., Cheung, W. W. L., Kairo, J. G., Arístegui, J., Guinder, V. A.,
 968 Hallberg, R., ... Williamson, P. (2022). Changing Ocean, Marine Ecosys-
 969 tems, and Dependent Communities. In *The Ocean and Cryosphere in a*
 970 *Changing Climate: Special Report of the Intergovernmental Panel on Cli-*
 971 *mate Change* (pp. 447–588). Cambridge: Cambridge University Press. doi:
 972 10.1017/9781009157964.007
- 973 Bopp, L., Le Quéré, C., Heimann, M., Manning, A. C., & Monfray, P. (2002).
 974 Climate-induced oceanic oxygen fluxes: Implications for the contempo-
 975 rary carbon budget. *Global Biogeochemical Cycles*, 16(2), 6-1-6-13. doi:
 976 10.1029/2001GB001445
- 977 Bopp, L., Resplandy, L., Orr, J. C., Doney, S. C., Dunne, J. P., Gehlen, M., ...
 978 Vichi, M. (2013). Multiple stressors of ocean ecosystems in the 21st cen-
 979 tury: Projections with CMIP5 models. *Biogeosciences*, 10(10), 6225–6245. doi:
 980 10.5194/bg-10-6225-2013
- 981 Bopp, L., Resplandy, L., Untersee, A., Le Mezo, P., & Kageyama, M. (2017). Ocean
 982 (de)oxygenation from the Last Glacial Maximum to the twenty-first cen-
 983 tury: Insights from Earth System models. *Philosophical Transactions of the*
 984 *Royal Society A: Mathematical, Physical and Engineering Sciences*, 375(2102),
 985 20160323. doi: 10.1098/rsta.2016.0323
- 986 Brandt, P., Bange, H. W., Banyte, D., Dengler, M., Didwischus, S.-H., Fischer, T.,
 987 ... Visbeck, M. (2015). On the role of circulation and mixing in the ventilation
 988 of oxygen minimum zones with a focus on the eastern tropical North Atlantic.
 989 *Biogeosciences*, 12(2), 489–512. doi: 10.5194/bg-12-489-2015
- 990 Breitburg, D., Levin, L. A., Oschlies, A., Grégoire, M., Chavez, F. P., Conley, D. J.,
 991 ... Zhang, J. (2018). Declining oxygen in the global ocean and coastal waters.
 992 *Science*, 359(6371), eaam7240. doi: 10.1126/science.aam7240
- 993 Broecker, W. S., & Peng, T.-H. (1982). Tracers in the Sea. *Lamont-Doherty Geolog-*
 994 *ical Observatory, Columbia University Palisades, New York*, 24(3), b1-b2. doi:
 995 10.1017/S0033822200005221

- 996 Buchanan, P. J., & Tagliabue, A. (2021). The Regional Importance of Oxygen De-
 997 mand and Supply for Historical Ocean Oxygen Trends. *Geophysical Research*
 998 *Letters*, 48(20), e2021GL094797. doi: 10.1029/2021GL094797
- 999 Busecke, J. J. M., Resplandy, L., Ditkovsky, S. J., & John, J. G. (2022). Diverging
 1000 Fates of the Pacific Ocean Oxygen Minimum Zone and Its Core in a Warming
 1001 World. *AGU Advances*, 3(6), e2021AV000470. doi: 10.1029/2021AV000470
- 1002 Chamberlain, M. A., Matear, R. J., Holzer, M., Bi, D., & Marsland, S. J. (2019).
 1003 Transport matrices from standard ocean-model output and quantifying cir-
 1004 culation response to climate change. *Ocean Modelling*, 135, 1-13. doi:
 1005 10.1016/j.ocemod.2019.01.005
- 1006 Chen, J.-J., Swart, N. C., Beadling, R., Cheng, X., Hattermann, T., Jüling, A., ...
 1007 Thomas, M. (2023). Reduced Deep Convection and Bottom Water Formation
 1008 Due To Antarctic Meltwater in a Multi-Model Ensemble. *Geophysical Research*
 1009 *Letters*, 50(24), e2023GL106492. doi: 10.1029/2023GL106492
- 1010 Cheng, L., von Schuckmann, K., Abraham, J. P., Trenberth, K. E., Mann, M. E.,
 1011 Zanna, L., ... Lin, X. (2022). Past and future ocean warming. *Nature Reviews*
 1012 *Earth & Environment*, 3(11), 776–794. doi: 10.1038/s43017-022-00345-1
- 1013 Cliff, E., Khatiwala, S., & Schmittner, A. (2021). Glacial deep ocean deoxygena-
 1014 tion driven by biologically mediated air-sea disequilibrium. *Nature Geoscience*,
 1015 14(1), 43–50. doi: 10.1038/s41561-020-00667-z
- 1016 Couespe, D., Lévy, M., & Bopp, L. (2019). Major Contribution of Reduced
 1017 Upper Ocean Oxygen Mixing to Global Ocean Deoxygenation in an Earth
 1018 System Model. *Geophysical Research Letters*, 46(21), 12239–12249. doi:
 1019 10.1029/2019GL084162
- 1020 Danisch, S., & Krumbiegel, J. (2021). Makie.jl: Flexible high-performance data vi-
 1021 sualization for Julia. *Journal of Open Source Software*, 6(65), 3349. doi: 10
 1022 .21105/joss.03349
- 1023 de Boyer Montégut, C., Madec, G., Fischer, A. S., Lazar, A., & Iudicone, D. (2004).
 1024 Mixed layer depth over the global ocean: An examination of profile data and a
 1025 profile-based climatology. *Journal of Geophysical Research: Oceans*, 109(C12).
 1026 doi: 10.1029/2004JC002378
- 1027 de Lavergne, C., Palter, J. B., Galbraith, E. D., Bernardello, R., & Marinov, I.
 1028 (2014). Cessation of deep convection in the open Southern Ocean under an-

- 1029 thropogenic climate change. *Nature Climate Change*, 4(4), 278–282. doi:
1030 10.1038/nclimate2132

1031 Deutsch, C., Emerson, S., & Thompson, L. (2006). Physical-biological interactions
1032 in North Pacific oxygen variability. *Journal of Geophysical Research: Oceans*,
1033 111(C9). doi: 10.1029/2005JC003179

1034 Deutsch, C., Ferrel, A., Seibel, B., Pörtner, H.-O., & Huey, R. B. (2015). Climate
1035 change tightens a metabolic constraint on marine habitats. *Science*, 348(6239),
1036 1132–1135. doi: 10.1126/science.aaa1605

1037 Deutsch, C., Penn, J. L., & Lucey, N. (2024). Climate, Oxygen, and the Future of
1038 Marine Biodiversity. *Annual Review of Marine Science*, 16(1), null. doi: 10.
1039 .1146/annurev-marine-040323-095231

1040 DeVries, T., & Deutsch, C. (2014). Large-scale variations in the stoichiometry of ma-
1041 rine organic matter respiration. *Nature Geoscience*, 7, 890–894. doi: 10.1038/
1042 NGEO2300

1043 Diaz, R. J., & Rosenberg, R. (2008). Spreading Dead Zones and Consequences
1044 for Marine Ecosystems. *Science*, 321(5891), 926–929. doi: 10.1126/science
1045 .1156401

1046 Doney, S. C., & Bullister, J. L. (1992). A chlorofluorocarbon section in the east-
1047 ern North Atlantic. *Deep Sea Research Part A. Oceanographic Research Pa-*
1048 *pers*, 39(11), 1857–1883. doi: 10.1016/0198-0149(92)90003-C

1049 Duteil, O., Koeve, W., Oschlies, A., Bianchi, D., Galbraith, E., Kriest, I., & Matear,
1050 R. (2013). A novel estimate of ocean oxygen utilisation points to a reduced
1051 rate of respiration in the ocean interior. *Biogeosciences*, 10(11), 7723–7738.
1052 doi: 10.5194/bg-10-7723-2013

1053 Earle, S. A., Wright, D. J., Joye, S., Laffoley, D., Baxter, J., Safina, C., & Elkus, P.
1054 (2018, March). Ocean deoxygenation: Time for action. *Science*, 359(6383),
1055 1475–1476. doi: 10.1126/science.aat0167

1056 Eggleston, S., & Galbraith, E. D. (2018). The devil's in the disequilibrium: Multi-
1057 component analysis of dissolved carbon and oxygen changes under a broad
1058 range of forcings in a general circulation model. *Biogeosciences*, 15(12),
1059 3761–3777. doi: 10.5194/bg-15-3761-2018

1060 Ekau, W., Auel, H., Pörtner, H.-O., & Gilbert, D. (2010). Impacts of hy-
1061 poxia on the structure and processes in pelagic communities (zooplank-

- ton, macro-invertebrates and fish). *Biogeosciences*, 7(5), 1669–1699. doi: 10.5194/bg-7-1669-2010
- Espinoza-Morriberón, D., Echevin, V., Gutiérrez, D., Tam, J., Graco, M., Ledesma, J., & Colas, F. (2021). Evidences and drivers of ocean deoxygenation off Peru over recent past decades. *Scientific Reports*, 11(1), 20292. doi: 10.1038/s41598-021-99876-8
- Falkowski, P. G., & Godfrey, L. V. (2008). Electrons, life and the evolution of Earth's oxygen cycle. *Philosophical Transactions of the Royal Society B: Biological Sciences*, 363(1504), 2705–2716. doi: 10.1098/rstb.2008.0054
- Feely, R. A., Sabine, C. L., Schlitzer, R., Bullister, J. L., Mecking, S., & Greeley, D. (2004). Oxygen Utilization and Organic Carbon Remineralization in the Upper Water Column of the Pacific Ocean. *Journal of Oceanography*, 60(1), 45–52. doi: 10.1023/B:JOCE.0000038317.01279.aa
- Franco, A. C., Kim, H., Frenzel, H., Deutsch, C., Ianson, D., Sumaila, U. R., & Tortell, P. D. (2022). Impact of warming and deoxygenation on the habitat distribution of Pacific halibut in the Northeast Pacific. *Fisheries Oceanography*, 31(6), 601–614. doi: 10.1111/fog.12610
- Frölicher, T. L., Aschwanden, M. T., Gruber, N., Jaccard, S. L., Dunne, J. P., & Paynter, D. (2020). Contrasting Upper and Deep Ocean Oxygen Response to Protracted Global Warming. *Global Biogeochemical Cycles*, 34(8), e2020GB006601. doi: 10.1029/2020GB006601
- Fu, W., Bardin, A., & Primeau, F. W. (2018). Tracing ventilation source of tropical pacific oxygen minimum zones with an adjoint global ocean transport model. *Deep Sea Research Part I: Oceanographic Research Papers*, 139, 95–103. doi: 10.1016/j.dsr.2018.07.017
- Gallo, N. D., & Levin, L. A. (2016). Chapter Three - Fish Ecology and Evolution in the World's Oxygen Minimum Zones and Implications of Ocean Deoxygenation. In B. E. Curry (Ed.), *Advances in Marine Biology* (Vol. 74, pp. 117–198). Academic Press. doi: 10.1016/bs.amb.2016.04.001
- Gnanadesikan, A., Dunne, J. P., & John, J. (2012). Understanding why the volume of suboxic waters does not increase over centuries of global warming in an Earth System Model. *Biogeosciences*, 9(3), 1159–1172. doi: 10.5194/bg-9-1159-2012

- 1095 Graco, M. I., Purca, S., Dewitte, B., Castro, C. G., Morón, O., Ledesma, J., ...
1096 Gutiérrez, D. (2017). The OMZ and nutrient features as a signature of in-
1097 terannual and low-frequency variability in the Peruvian upwelling system.
1098 *Biogeosciences*, 14(20), 4601–4617. doi: 10.5194/bg-14-4601-2017
- 1099 Gunn, K. L., Rintoul, S. R., England, M. H., & Bowen, M. M. (2023). Recent re-
1100 duced abyssal overturning and ventilation in the Australian Antarctic Basin.
1101 *Nature Climate Change*, 13(6), 537–544. doi: 10.1038/s41558-023-01667-8
- 1102 Helm, K. P., Bindoff, N. L., & Church, J. A. (2011). Observed decreases in oxy-
1103 gen content of the global ocean. *Geophysical Research Letters*, 38(23). doi: 10
1104 .1029/2011GL049513
- 1105 Heuzé, C., Heywood, K. J., Stevens, D. P., & Ridley, J. K. (2013). Southern Ocean
1106 bottom water characteristics in CMIP5 models. *Geophysical Research Letters*,
1107 40(7), 1409–1414. doi: 10.1002/grl.50287
- 1108 Heuzé, C., Heywood, K. J., Stevens, D. P., & Ridley, J. K. (2015). Changes in
1109 Global Ocean Bottom Properties and Volume Transports in CMIP5 Models
1110 under Climate Change Scenarios. *Journal of Climate*, 28(8), 2917–2944. doi:
1111 10.1175/JCLI-D-14-00381.1
- 1112 Hofmann, A. F., Peltzer, E. T., Walz, P. M., & Brewer, P. G. (2011). Hypoxia by
1113 degrees: Establishing definitions for a changing ocean. *Deep Sea Research Part*
1114 *I: Oceanographic Research Papers*, 58(12), 1212–1226. doi: 10.1016/j.dsr.2011
1115 .09.004
- 1116 Holzer, M. (2022). The fate of oxygen in the ocean and its sensitivity to lo-
1117 cal changes in biological production. *Journal of Geophysical Research:*
1118 *Oceans*, 127(8), e2022JC018802. (e2022JC018802 2022JC018802) doi:
1119 10.1029/2022JC018802
- 1120 Holzer, M., Chamberlain, M. A., & Matear, R. J. (2020). Climate-driven changes
1121 in the ocean's ventilation pathways and time scales diagnosed from transport
1122 matrices. *Journal of Geophysical Research: Oceans*, 125(10), e2020JC016414.
1123 (e2020JC016414 10.1029/2020JC016414) doi: 10.1029/2020JC016414
- 1124 Holzer, M., DeVries, T., & de Lavergne, C. (2021). Diffusion controls the ventilation
1125 of a Pacific Shadow Zone above abyssal overturning. *Nature Communications*,
1126 12(1), 4348. doi: 10.1038/s41467-021-24648-x
- 1127 Holzer, M., & Hall, T. M. (2000). Transit-Time and Tracer-Age Distributions in

- 1128 Geophysical Flows. *Journal of the Atmospheric Sciences*, 57(21), 3539–3558.
 1129 doi: 10.1175/1520-0469(2000)057<3539:TTATAD>2.0.CO;2
- 1130 Ito, T. (2022). Optimal interpolation of global dissolved oxygen: 1965–2015. *Geo-*
 1131 *science Data Journal*, 9(1), 167–176. doi: 10.1002/gdj3.130
- 1132 Ito, T., Follows, M. J., & Boyle, E. A. (2004). Is AOU a good measure of respi-
 1133 ration in the oceans? *Geophysical Research Letters*, 31(17). doi: 10.1029/
 1134 2004GL020900
- 1135 Ito, T., Garcia, H. E., Wang, Z., Minobe, S., Long, M. C., Cebrian, J., ... Deutsch,
 1136 C. A. (2024). Underestimation of multi-decadal global O₂ loss due to
 1137 an optimal interpolation method. *Biogeosciences*, 21(3), 747–759. doi:
 1138 10.5194/bg-21-747-2024
- 1139 Ito, T., Minobe, S., Long, M. C., & Deutsch, C. (2017). Upper ocean O₂ trends:
 1140 1958–2015. *Geophysical Research Letters*, 44(9), 4214–4223. doi: 10.1002/
 1141 2017GL073613
- 1142 Ito, T., Takano, Y., Deutsch, C., & Long, M. C. (2022). Sensitivity of Global
 1143 Ocean Deoxygenation to Vertical and Isopycnal Mixing in an Ocean Biogeo-
 1144 chemistry Model. *Global Biogeochemical Cycles*, 36(4), e2021GB007151. doi:
 1145 10.1029/2021GB007151
- 1146 Jin, X., Najjar, R. G., Louanchi, F., & Doney, S. C. (2007). A modeling study of the
 1147 seasonal oxygen budget of the global ocean. *Journal of Geophysical Research:*
 1148 *Oceans*, 112(C5). doi: 10.1029/2006JC003731
- 1149 Keeling, R. F., & Garcia, H. E. (2002). The change in oceanic O₂ inventory associ-
 1150 ated with recent global warming. *Proceedings of the National Academy of Sci-*
 1151 *ences*, 99(12), 7848–7853. doi: 10.1073/pnas.122154899
- 1152 Keeling, R. F., Körtzinger, A., & Gruber, N. (2010). Ocean Deoxygenation in a
 1153 Warming World. *Annual Review of Marine Science*, 2(1), 199–229. doi: 10
 1154 .1146/annurev.marine.010908.163855
- 1155 Koeve, W., & Kähler, P. (2016). Oxygen utilization rate (OUR) underestimates
 1156 ocean respiration: A model study. *Global Biogeochemical Cycles*, 30(8),
 1157 1166–1182. doi: 10.1002/2015GB005354
- 1158 Kwiatkowski, L., Torres, O., Bopp, L., Aumont, O., Chamberlain, M., Christian,
 1159 J. R., ... Ziehn, T. (2020). Twenty-first century ocean warming, acidifica-
 1160 tion, deoxygenation, and upper-ocean nutrient and primary production decline

- from CMIP6 model projections. *Biogeosciences*, 17(13), 3439–3470. doi: 10.5194/bg-17-3439-2020
- Laffoley, D., & Baxter, J. M. (2019). *Ocean deoxygenation: Everyone's problem: Causes, impacts, consequences and solutions: Summary for Policy Makers* (Report). Gland: International Union for Conservation of Nature (IUCN). doi: 10.2305/IUCN.CH.2019.14.en
- Lauvset, S. K., Key, R. M., Olsen, A., van Heuven, S., Velo, A., Lin, X., ... Wa-telet, S. (2016). A new global interior ocean mapped climatology: The 1×1 GLODAP version 2. *Earth System Science Data*, 8(2), 325–340. doi: 10.5194/essd-8-325-2016
- Levin, L. A. (2018). Manifestation, Drivers, and Emergence of Open Ocean De-oxygenation. *Annual Review of Marine Science*, 10, 229–260. doi: 10.1146/annurev-marine-121916-063359
- Li, Q., England, M. H., Hogg, A. M., Rintoul, S. R., & Morrison, A. K. (2023). Abyssal ocean overturning slowdown and warming driven by Antarctic meltwater. *Nature*, 615(7954), 841–847. doi: 10.1038/s41586-023-05762-w
- Long, M. C., Ito, T., & Deutsch, C. (2019). Oxygen projections for the future. In *Ocean deoxygenation: Everyone's problem — causes, impacts, consequences and solutions* (pp. 171–211). Gland, Switzerland: IUCN.
- Marsland, S., Bi, D., Uotila, P., Fiedler, R., Griffies, S., Lorbacher, K., ... Hirst, A. (2013). Configuration and spin-up of ACCESS-CM2, the new generation Australian Community Climate and Earth System Simulator Coupled Model. *Australian Meteorological and Oceanographic Journal*, 63, 101–119. doi: 10.22499/2.6301.007
- Matear, R. J., & Hirst, A. C. (2003). Long-term changes in dissolved oxygen concentrations in the ocean caused by protracted global warming. *Global Biogeochemical Cycles*, 17(4). doi: 10.1029/2002GB001997
- Matear, R. J., Hirst, A. C., & McNeil, B. I. (2000). Changes in dissolved oxygen in the Southern Ocean with climate change. *Geochemistry, Geophysics, Geosystems*, 1(11). doi: 10.1029/2000GC000086
- McCormick, L. R., & Levin, L. A. (2017). Physiological and ecological implications of ocean deoxygenation for vision in marine organisms. *Philosophical Transactions of the Royal Society A: Mathematical, Physical and Engineering Sciences*,

- 1194 375(2102), 20160322. doi: 10.1098/rsta.2016.0322
- 1195 Meinshausen, M., Nicholls, Z. R. J., Lewis, J., Gidden, M. J., Vogel, E., Freund, M.,
 1196 ... Wang, R. H. J. (2020). The shared socio-economic pathway (ssp) green-
 1197 house gas concentrations and their extensions to 2500. *Geoscientific Model
 Development*, 13(8), 3571–3605. doi: 10.5194/gmd-13-3571-2020
- 1198 Meinshausen, M., Smith, S. J., Calvin, K., Daniel, J. S., Kainuma, M. L. T., Lamar-
 1200 que, J.-F., ... van Vuuren, D. P. (2011). The RCP greenhouse gas concentra-
 1201 tions and their extensions from 1765 to 2300. *Climatic Change*, 109(1), 213.
 1202 doi: 10.1007/s10584-011-0156-z
- 1203 Mongwe, P., Long, M., Ito, T., Deutsch, C., & Santana-Falcón, Y. (under review).
 1204 Climatic Controls on Metabolic Constraints in the Ocean. *EGUsphere*, 1–29.
 1205 doi: 10.5194/egusphere-2023-2822
- 1206 Moore, J. K., Fu, W., Primeau, F. W., Britten, G. L., Lindsay, K., Long, M.,
 1207 ... Randerson, J. T. (2018). Sustained climate warming drives declin-
 1208 ing marine biological productivity. *Science*, 359(6380), 1139-1143. doi:
 1209 10.1126/science.aa06379
- 1210 Morée, A. L., Clarke, T. M., Cheung, W. W. L., & Frölicher, T. L. (2023). Impact of
 1211 deoxygenation and warming on global marine species in the 21st century. *Bio-
 1212 geosciences*, 20(12), 2425–2454. doi: 10.5194/bg-20-2425-2023
- 1213 Oschlies, A. (2021). A committed fourfold increase in ocean oxygen loss. *Nature
 Communications*, 12(1), 2307. doi: 10.1038/s41467-021-22584-4
- 1214 Oschlies, A., Brandt, P., Stramma, L., & Schmidtko, S. (2018). Drivers and mech-
 1215 anisms of ocean deoxygenation. *Nature Geoscience*, 11(7), 467–473. doi: 10
 1216 .1038/s41561-018-0152-2
- 1217 Oschlies, A., Koeve, W., Landolfi, A., & Kähler, P. (2019). Loss of fixed nitro-
 1218 gen causes net oxygen gain in a warmer future ocean. *Nature Communications*,
 1219 10(1), 2805. doi: 10.1038/s41467-019-10813-w
- 1220 Palter, J. B., & Trossman, D. S. (2018). The Sensitivity of Future Ocean Oxygen to
 1221 Changes in Ocean Circulation. *Global Biogeochemical Cycles*, 32(5), 738–751.
 1222 doi: 10.1002/2017GB005777
- 1223 Pascal, L., Cool, J., Archambault, P., Calosi, P., Cuenca, A. L. R., Mucci, A. O.,
 1224 & Chaillou, G. (2023). Ocean deoxygenation caused non-linear responses in
 1225 the structure and functioning of benthic ecosystems. *Global Change Biology*,

- 1227 *n/a(n/a)*, e16994. doi: 10.1111/gcb.16994
- 1228 Pasquier, B., Holzer, M., & Chamberlain, M. A. (2023, December). The ocean's bi-
1229 ological and preformed carbon pumps in future steady-state climate scenarios.
1230 *EGUsphere*, 1–41. doi: 10.5194/egusphere-2023-2525
- 1231 Pasquier, B., Holzer, M., Chamberlain, M. A., Matear, R. J., Bindoff, N. L., &
1232 Primeau, F. W. (2023). Optimal parameters for the ocean's nutrient,
1233 carbon, and oxygen cycles compensate for circulation biases but replumb
1234 the biological pump. *Biogeosciences (Online)*, 20(14), 2985–3009. doi:
1235 10.5194/bg-20-2985-2023
- 1236 Pitcher, G. C., Aguirre-Velarde, A., Breitburg, D., Cardich, J., Carstensen, J.,
1237 Conley, D. J., ... Zhu, ZY. (2021). System controls of coastal and open
1238 ocean oxygen depletion. *Progress in Oceanography*, 197, 102613. doi:
1239 10.1016/j.pocean.2021.102613
- 1240 Plattner, G.-K., Joos, F., Stocker, T. F., & Marchal, O. (2001). Feedback mecha-
1241 nisms and sensitivities of ocean carbon uptake under global warming. *Tellus B:*
1242 *Chemical and Physical Meteorology*, 53(5), 564–592. doi: 10.3402/tellusb.v53i5
1243 .16637
- 1244 Primeau, F. W. (2005). Characterizing transport between the surface mixed
1245 layer and the ocean interior with a forward and adjoint global ocean trans-
1246 port model. *Journal of Physical Oceanography*, 35(4), 545–564. doi:
1247 10.1175/JPO2699.1
- 1248 Purich, A., & England, M. H. (2023). Projected Impacts of Antarctic Meltwa-
1249 ter Anomalies over the Twenty-First Century. *Journal of Climate*, 36(8),
1250 2703–2719. doi: 10.1175/JCLI-D-22-0457.1
- 1251 Purich, A., England, M. H., Cai, W., Sullivan, A., & Durack, P. J. (2018). Impacts
1252 of Broad-Scale Surface Freshening of the Southern Ocean in a Coupled Climate
1253 Model. *Journal of Climate*, 31(7), 2613–2632. doi: 10.1175/JCLI-D-17-0092.1
- 1254 Riahi, K., van Vuuren, D. P., Kriegler, E., Edmonds, J., O'Neill, B. C., Fujimori, S.,
1255 ... Tavoni, M. (2017). The shared socioeconomic pathways and their energy,
1256 land use, and greenhouse gas emissions implications: An overview. *Global*
1257 *Environmental Change*, 42, 153–168. doi: 10.1016/j.gloenvcha.2016.05.009
- 1258 Roach, C. J., & Bindoff, N. L. (2023). Developing a New Oxygen Atlas of the
1259 World's Oceans Using Data Interpolating Variational Analysis. *Jour-*

- 1260 *nal of Atmospheric and Oceanic Technology*, 40(11), 1475–1491. doi:
1261 10.1175/JTECH-D-23-0007.1

1262 Rogers, A. D. (2000). The role of the oceanic oxygen minima in generating biodiver-
1263 sity in the deep sea. *Deep Sea Research Part II: Topical Studies in Oceanogra-*
1264 *phy*, 47(1), 119–148. doi: 10.1016/S0967-0645(99)00107-1

1265 Russell, J. L., & Dickson, A. G. (2003). Variability in oxygen and nutrients in South
1266 Pacific Antarctic Intermediate Water. *Global Biogeochemical Cycles*, 17(2).
1267 doi: 10.1029/2000GB001317

1268 Sarmiento, J. L., Herbert, T. D., & Toggweiler, J. R. (1988). Causes of anoxia in
1269 the world ocean. *Global Biogeochemical Cycles*, 2(2), 115–128. doi: 10.1029/
1270 GB002i002p00115

1271 Sato, K. N., Levin, L. A., & Schiff, K. (2017). Habitat compression and expansion of
1272 sea urchins in response to changing climate conditions on the California conti-
1273 nental shelf and slope (1994–2013). *Deep Sea Research Part II: Topical Studies*
1274 *in Oceanography*, 137, 377–389. doi: 10.1016/j.dsr2.2016.08.012

1275 Schmidtko, S., Stramma, L., & Visbeck, M. (2017). Decline in global oceanic oxy-
1276 gen content during the past five decades. *Nature*, 542(7641), 335–339. doi: 10.
1277 .1038/nature21399

1278 Schmittner, A., Oschlies, A., Matthews, H. D., & Galbraith, E. D. (2008). Future
1279 changes in climate, ocean circulation, ecosystems, and biogeochemical cycling
1280 simulated for a business-as-usual co2 emission scenario until year 4000 ad.
1281 *Global Biogeochemical Cycles*, 22(1). doi: 10.1029/2007GB002953

1282 Seibel, B. A. (2011). Critical oxygen levels and metabolic suppression in oceanic
1283 oxygen minimum zones. *Journal of Experimental Biology*, 214(2), 326–336. doi:
1284 10.1242/jeb.049171

1285 Shaffer, G., Olsen, S. M., & Pedersen, J. O. P. (2009). Long-term ocean oxygen de-
1286 pletion in response to carbon dioxide emissions from fossil fuels. *Nature Geo-*
1287 *science*, 2(2), 105–109. doi: 10.1038/ngeo420

1288 Sonnerup, R. E., Mecking, S., & Bullister, J. L. (2013). Transit time distributions
1289 and oxygen utilization rates in the Northeast Pacific Ocean from chlorofluo-
1290 rocarbons and sulfur hexafluoride. *Deep Sea Research Part I: Oceanographic*
1291 *Research Papers*, 72, 61–71. doi: 10.1016/j.dsr.2012.10.013

1292 Sonnerup, R. E., Mecking, S., Bullister, J. L., & Warner, M. J. (2015). Transit time

- 1293 distributions and oxygen utilization rates from chlorofluorocarbons and sulfur
 1294 hexafluoride in the Southeast Pacific Ocean. *Journal of Geophysical Research: Oceans*, 120(5), 3761–3776. doi: 10.1002/2015JC010781
- 1295 Srokosz, M. A., & Bryden, H. L. (2015). Observing the Atlantic Meridional Overturning Circulation yields a decade of inevitable surprises. *Science*, 348(6241), 1255575. doi: 10.1126/science.1255575
- 1296 Stramma, L., Prince, E. D., Schmidtko, S., Luo, J., Hoolihan, J. P., Visbeck, M., ...
 1297 Körtzinger, A. (2012). Expansion of oxygen minimum zones may reduce available habitat for tropical pelagic fishes. *Nature Climate Change*, 2(1), 33–37.
 1298 doi: 10.1038/nclimate1304
- 1299 Takano, Y., Ilyina, T., Tjiputra, J., Eddebbar, Y. A., Berthet, S., Bopp, L., ... Yool,
 1300 A. (2023). Simulations of ocean deoxygenation in the historical era: Insights from forced and coupled models. *Frontiers in Marine Science*, 10.
- 1301 Thomas, J. L., Waugh, D. W., & Gnanadesikan, A. (2020). Relationship between
 1302 Age and Oxygen along Line W in the Northwest Atlantic Ocean. *Ocean Science Journal*, 55(2), 203–217. doi: 10.1007/s12601-020-0019-5
- 1303 Vaquer-Sunyer, R., & Duarte, C. M. (2008). Thresholds of hypoxia for marine
 1304 biodiversity. *Proceedings of the National Academy of Sciences*, 105(40),
 1305 15452–15457. doi: 10.1073/pnas.0803833105
- 1306 Wanninkhof, R. (2014). Relationship between wind speed and gas exchange over the
 1307 ocean revisited. *Limnology and Oceanography: Methods*, 12(6), 351–362. doi:
 1308 10.4319/lom.2014.12.351
- 1309 Warner, M. J., Bullister, J. L., Wisegarver, D. P., Gammon, R. H., & Weiss, R. F.
 1310 (1996). Basin-wide distributions of chlorofluorocarbons CFC-11 and CFC-12
 1311 in the North Pacific: 1985–1989. *Journal of Geophysical Research: Oceans*,
 1312 101(C9), 20525–20542. doi: 10.1029/96JC01849
- 1313 Whitney, F. A., Freeland, H. J., & Robert, M. (2007). Persistently declining oxygen levels in the interior waters of the eastern subarctic Pacific. *Progress in
 1314 Oceanography*, 75(2), 179–199. doi: 10.1016/j.pocean.2007.08.007
- 1315 Wishner, K. F., Seibel, B. A., Roman, C., Deutsch, C., Outram, D., Shaw, C. T.,
 1316 ... Riley, S. (2018). Ocean deoxygenation and zooplankton: Very small
 1317 oxygen differences matter. *Science Advances*, 4(12), eaau5180. doi:
 1318 10.1126/sciadv.aau5180

- 1326 Wyrki, K. (1962). The oxygen minima in relation to ocean circulation. *Deep*
1327 *Sea Research and Oceanographic Abstracts*, 9(1), 11–23. doi: 10.1016/
1328 0011-7471(62)90243-7
- 1329 Zheng, Y., Schlosser, P., Swift, J. H., & Jones, E. P. (1997). Oxygen utilization rates
1330 in the Nansen Basin, Arctic Ocean: Implications for new production. *Deep Sea*
1331 *Research Part I: Oceanographic Research Papers*, 44(12), 1923–1943. doi: 10
1332 .1016/S0967-0637(97)00046-0